



National Technical University of Athens
School of Mechanical Engineering
Fluids Department
Parallel CFD & Optimization Unit

Modeling & Optimization of Gas Diffusion Layer in Fuel Cells, in the OpenFOAM environment

Diploma Thesis

Petros P. Lamprinidis

Academic Supervisor :
Kyriakos C. Giannakoglou, Professor NTUA

Industrial Supervisor :
Dr. Konstantinos Gkagkas, Expert, Toyota Motor Europe

Athens, February 2021

Acknowledgements

First of all, I would like to express my deepest gratitude to my professor, K.C. Giannakoglou. For the past years, he has been an inspiring figure not only as a scientist but also as a teacher. I consider myself very fortunate to have been able to work under his academic supervision on this interesting topic.

Secondly, I would like to wholeheartedly thank my industrial supervisor Dr. K. Gkagkas as well as Dr. G. Turon. During my internship at Toyota Motor Europe, but also after, their guidance and advice have been indisputably of great importance. Their enthusiasm towards science and engineering as well as their constant eagerness to discuss new and exciting ideas have been most inspiring for me. I would also like to thank the rest of the Advanced Technology Division for all the fruitful discussions they provided during my stay at Belgium.

I would also like to thank all the members of the research team of PCOpt/NTUA for always being available to help when needed. In particular, I would like to express my most sincere gratitude to Dr. K. Gkaragkounis and Dr. V. Asouti for always being eager and happy to share some of their knowledge.

Last but not least, I would like to thank my parents, Periklis and Sonia, for always being there for me with their love and support and my friends, the three Gs, for their companionship and for being individually unique, romantic and authentic.

In loving memory of my father, Periklis, the authentic seawolf.



National Technical University of Athens
School of Mechanical Engineering
Fluids Department
Parallel CFD & Optimization Unit

Modeling & Optimization of Gas Diffusion Layer in Fuel Cells, in the OpenFOAM environment

Diploma Thesis

Petros P. Lamprinidis

Academic Supervisor :
Kyriakos C. Giannakoglou, Professor NTUA

Industrial Supervisor :
Dr. Konstantinos Gkagkas, Expert Toyota Motor Europe

Athens, February 2021

Abstract

Fuel cells are gaining increasing research interest as an alternative clean and sustainable energy source to replace fossil fuels. In the automotive industry, proton exchange membrane (PEM) fuel cells are prevailing due to the high power density and low working temperatures. One of the components of the fuel cell that significantly affects its performance is the Gas Diffusion Layer (GDL), due to the various phenomena that take place there.

In this diploma thesis, the GDL of a PEM fuel cell is modeled and optimized with regards to its porosity. Nowadays, research is focusing on innovative ways to control the porosity distribution of the GDL. Porosity currently used in the GDL is constant. It is important, therefore, to numerically study whether a varying porosity distribution has a significant positive effect on the fuel cell performance.

The CFD model that is used for the PEM fuel cell is selected from the literature, after an appropriate survey. It consists of modified Navier-Stokes equations to also account for the various electrical, thermal and chemical phenomena, an extra equation accounting for the two-phase flow that takes place, and an equation for the

conservation of chemical species. The model is developed and simulated in the OpenFOAM environment.

On the other hand, the optimization is performed using the evolutionary algorithm based optimization software EASY of NTUA. The porosity distribution that is used is linear in all three directions to be realistically manufacturable even with porosity controlling manufacturing. It is shown that porosity non-constant distributions are indeed favorable and the porosity along all three directions has an impact on performance. The preferred distributions however depend significantly on the operating conditions.

Major part in this diploma thesis was carried out in the premises of Toyota Motor Europe in Brussels, Belgium, during a 6 month long internship.



Εθνικό Μετσόβιο Πολυτεχνείο
Σχολή Μηχανολόγων Μηχανικών
Τομέας Ρευστών
Μονάδα Παράλληλης Υπολογιστικής Ρευστοδυναμικής
& Βελτιστοποίησης

Μοντελοποίηση & Βελτιστοποίηση Στρώματος Διάχυσης Αερίου Κυψελών Καυσίμου και Πορώδους στο OpenFOAM

Διπλωματική Εργασία

Πέτρος Π. Λαμπρινίδης

Επιβλέπων :

Κυριάκος Χ. Γιαννάκογλου, Καθηγητής ΕΜΠ

Βιομηχανικός Επιβλέπων :

Δρ. Κωνσταντίνος Γκαγκάς, Toyota Motor Europe

Αθήνα, Φεβρουάριος 2021

Περίληψη

Οι κυψέλες καυσίμου αποκτούν αυξανόμενο ερευνητικό ενδιαφέρον ως εναλλακτική πηγή καθαρής και βιώσιμης ενέργειας για να αντικαταστήσουν τα ορυκτά καύσιμα. Στην αυτοκινητοβιομηχανία, επικρατούν οι κυψέλες καυσίμου μεμβράνης ανταλλαγής πρωτονίων (Proton Exchange Membrane, PEM) λόγω της υψηλής πυκνότητας ισχύος και των χαμηλών θερμοκρασιών λειτουργίας. Ένα από τα συστατικά στοιχεία της κυψέλης καυσίμου που έχει εξαιρετική επιρροή στην απόδοση είναι το Στρώμα Διάχυσης Αερίου (Gas Diffusion Layer, GDL) λόγω των ποικίλων φαινομένων που λαμβάνουν χώρα εκεί.

Σε αυτήν τη διπλωματική εργασία, το GDL μίας κυψέλης καυσίμου PEM μοντελοποιείται και βελτιστοποιείται ως προς το πορώδες του. Πρόσφατες έρευνες έχουν μελετήσει καινοτόμους τρόπους για τον έλεγχο της κατανομής πορώδους του GDL κατά την κατασκευή. Το πορώδες που χρησιμοποιείται σήμερα στο GDL είναι σταθερό. Είναι σημαντικό, επομένως, να μελετηθεί αριθμητικά εάν μια μη-σταθερή κατανομή πορώδους θα είχε ευνοϊκή επίδραση στην απόδοση της κυψέλης καυσίμου.

Το μαθηματικό μοντέλο ανάλυσης μιας δεδομένης κυψέλης καυσίμου PEM επιλέγεται από τη βιβλιογραφία. Αποτελείται από τις εξισώσεις Navier-Stokes που έχουν τροποποιηθεί ώστε να ληφθούν υπόψη τα διάφορα ηλεκτρικά, θερμικά και χημικά φαινόμενα, μια επιπλέον εξίσωση που αντιστοιχεί στη διφασική ροή που λαμβάνει χώρα και μια επιπλέον εξίσωση για τη διατήρηση των χημικών στοιχείων. Το μοντέλο αναπτύσσεται και προσομοιώνεται σε περιβάλλον OpenFOAM.

Η βελτιστοποίηση πραγματοποιείται, στη συνέχεια, χρησιμοποιώντας το λογισμικό EASY του EMPI το οποίο βασίζεται σε εξελικτικούς αλγόριθμους. Η κατανομή πορώδους που χρησιμοποιείται είναι γραμμική και στις τρεις κατευθύνσεις ώστε να είναι ρεαλιστικά κατασκευάσιμη ακόμη και με έλεγχο του πορώδους κατά την κατασκευή. Αποδεικνύεται ότι οι κατανομές πορώδους είναι πράγματι ευνοϊκές και το πορώδες και στις τρεις κατευθύνσεις επηρεάζει την απόδοση. Ωστόσο, οι προτιμώμενες κατανομές εξαρτώνται σημαντικά από τις συνθήκες λειτουργίας.

Το μεγαλύτερο τμήμα αυτής της διπλωματικής εργασίας πραγματοποιήθηκε στις εγκαταστάσεις της Toyota Motor Europe στις Βρυξέλλες του Βελγίου κατά τη διάρκεια εξαμηνιαίας πρακτικής άσκησης.

Acronyms

BPP	Bi-polar Plate
CFD	Computational Fluid Dynamics
CL	Catalyst Layer
EA	Evolutionary Algorithm
EASY	Evolutionary Algorithms SYstem
FC	Fuel Cell
GDL	Gas Diffusion Layer
GFC	Gas Flow Channel
MEA	Membrane Electrode Assembly
MPL	Microporous Layer
NTUA	National Technical University of Athens
PCopt	Parallel CFD & Optimization unit
PEM	Proton Exchange Membrane
TME	Toyota Motor Europe

Contents

Contents	i
1 Introduction	1
1.1 Fuel Cells	1
1.2 Fuel Cell Types	3
1.3 PEM Fuel Cells	4
1.4 Literature Survey	6
1.4.1 On Two-Phase Flow Modeling in GDLs	7
1.4.2 PEM Fuel Cell/GDL Modeling & Optimization Studies	8
1.4.3 Model and Software Selection	10
1.5 Scope and Structure of the Thesis	11
2 Model Description & Assesment	13
2.1 Geometry & Domains	13
2.2 Assumptions	16
2.3 Governing Equations	17
2.4 Constitutive Equations	20
2.5 Boundary Conditions	24
2.6 Reference Case Parameters Values & Operating Conditions	25
2.7 I-V Curve & Overpotentials	27
2.8 Discussion on the Reference Case Results	28
2.8.1 Gas Flow Channels Results	28
2.8.2 Gas Diffusion Layer Results	33
3 Variable Porosity & Manual Optimization	37
3.1 Parametric Study of Constant Porosity	37
3.2 Model Modifications for Variable Porosity	40
3.3 "Manual" Optimization	41

4	Optimization	45
4.1	Evolutionary Algorithms	45
4.1.1	EA-Based Optimization	46
4.1.2	EASY	48
4.2	3D Linear Porosity Distributions	48
4.3	Results	50
5	Overview and Conclusions	59
5.1	Overview	59
5.2	Conclusions	60
	Bibliography	i

Chapter 1

Introduction

1.1 Fuel Cells

The fossil fuels, e.g coal, oil, and natural gas, are the major energy sources, but are considered very dangerous from an environmental point of view. At the same time, the fear is often expressed that the rapid usage resulting in disappearance of fossil fuels will terminate the progress of increasing demands in many fields, including transportation. With the increasing interest of clean and sustainable energy to overcome the fears, fuel cells are attracting more and more attention from research.

A fuel cell is an electrochemical cell that converts the chemical energy of a fuel (often hydrogen) and an oxidizing agent (often oxygen) into electricity through a pair of reduction-oxidation reactions, meaning that a transfer of electrons takes place between the fuel and the oxidizing agent. All types of fuel cells consist of an anode, a cathode, and an electrolyte. At the anode a catalyst oxidizes the fuel that is supplied, usually hydrogen, turning the fuel into positively charged ions (most commonly a hydrogen proton) and a negatively charged electron. The electrolyte is a substance specifically designed so that ions can pass through it, but electrons cannot. The electrons travel through an external circuit creating the electric current. The ions travel through the electrolyte to the cathode. Once reaching the cathode, the ions are reunited with the electrons and the two react with a third supplied chemical, usually oxygen, to create water or carbon dioxide. Figure 1.1 shows a basic schematic of this entire process.

The anode and the cathode of a fuel cell generally consist of two separate components. The first component is the gas diffusion layer (GDL) which is the porous medium of the fuel cell. It serves in distributing the fluid flow evenly to the catalyst and also transferring heat and electrical charge. It also helps in removing excess

liquid water if present due to its hydrophobic design. The second component is the catalyst layer (CL) as described earlier. The anode catalyst is, often, fine platinum powder while the cathode catalyst is, often, nickel.

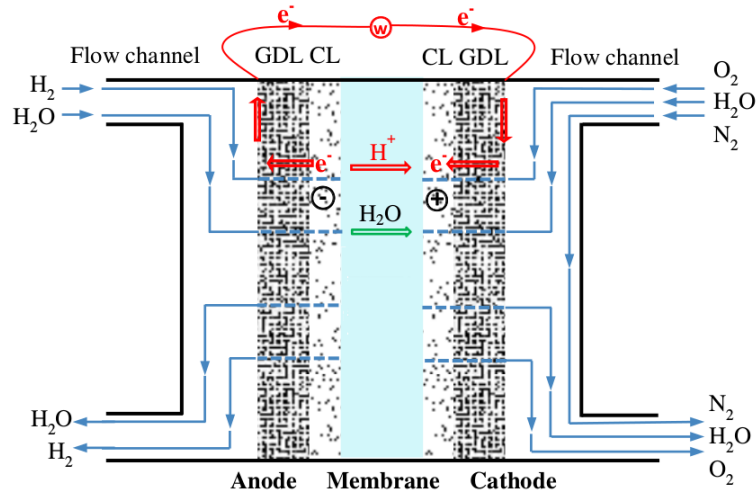


Figure 1.1: Schematic of the basic processes that occur in all types of fuel cells [24].

The voltage output of the fuel cell for a certain current density or load is often a measure of its general performance. A polarization or I-V curve expresses the fuel cell voltage output with regards to the current density. Figure 1.2 shows a typical I-V curve with all the voltage losses that occur. These losses can be categorized into three different types :

- Activation losses η_{act} due to reaction kinetics
- Ohmic losses η_{ohm} due to electrical resistance in the electrolyte and the other components
- Concentration losses η_{con} due to mass transport limitations

Lastly, to deliver the desired amount of energy, the fuel cells can be combined in series to yield higher voltage, and in parallel to allow a higher current to be supplied. Such a design is called a fuel cell stack. The cell surface area can also be increased, to allow higher current from each cell. The energy efficiency of a fuel cell is generally between 40 and 60%.

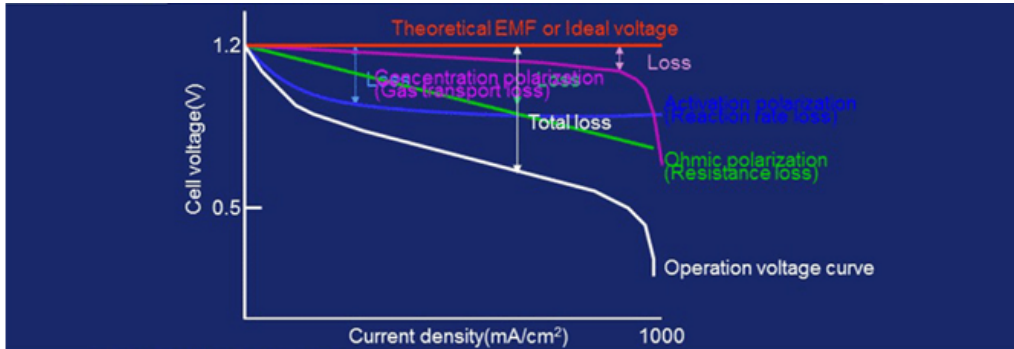


Figure 1.2: Typical I-V curve.

1.2 Fuel Cell Types

Even though all fuel cells work in the same general manner, they are divided in different types. The electrolyte substance is most commonly what defines the fuel cell type.

In **proton exchange membrane (PEM) fuel cells** [1] (previously called polymer electrolyte membrane fuel cells), a proton-conducting polymer membrane (typically nafflon) contains the electrolyte solution that separates the anode and cathode sides. The fuel used in PEM fuel cells is hydrogen and the operating temperature is typically around 100 °C. The low working temperatures along with the high power density these fuel cells provide, make them the most extensively used type of fuel cell and, nowadays, the main type of fuel cell in the automotive industry. PEM fuel cells also use bi-polar plates (BPPs), metal constructions which encompass both the anode and cathode, which help conduct electrical current from cell to cell, remove heat from the active area and prevent leakage of gases and coolant.

Phosphoric acid (PA) fuel cells [2] are a type of fuel cell that uses liquid phosphoric acid as an electrolyte and were the first fuel cells to be commercialized. These cells commonly work in temperatures of 150 to 200 °C. PA fuel cells have been used as stationary power generators and nowadays are finding application in large vehicles such as buses. A key disadvantage of these cells is the use of an acidic electrolyte as it increases the corrosion or oxidation of components exposed to phosphoric acid.

Solid acid (SA) fuel cells [3] are characterized by the use of a solid acid material as the electrolyte. At warmer temperatures some solid acids undergo a phase transition to become highly disordered "superprotonic" structures, which increases conductivity by several orders of magnitude. The first developed SA fuel cells used cesium hydrogen sulfate ($CsHSO_4$) while current SA fuel cell systems use cesium dihydrogen phosphate (CsH_2PO_4). Because of their compatibility with several types of fuel, SA fuel cells can be utilized in remote locations where other types of fuel

cells would be impractical and oftentimes find application in remote oil and gas as the power system of wellheads.

Solid oxide (SO) fuel cells [4] use a solid material, most commonly a ceramic material called yttria-stabilized zirconia (YSZ), as the electrolyte. They require high operating temperatures (800–1000 °C) and can be run on a variety of fuels including natural gas. SO fuel cells are unique since in those, negatively charged oxygen ions are transferred from the cathode to the anode contrary to the transfer of positive ions from anode to cathode in all other fuel cell types. The high operating temperature is largely due to the physical properties of the YSZ electrolyte as the ionic conductivity of YSZ is suitable for use only in those temperatures. SO fuel cells have a wide variety of applications, mainly as auxiliary power units in vehicles and stationary power generation units.

A few other types of fuel cells are also being researched and developed, their main difference being the electrolyte substance. However, these types of fuel cells are either on a developmental stage or they find too limited of an application and thus are not worth mentioning here.

1.3 PEM Fuel Cells

Typically a PEM fuel cell operates around 100 °C (usually 80 °C for low temperature PEM fuel cells and approximately 120 °C for high temperature PEM fuel cells). A sketch of a PEM fuel cell with the various transports and components is shown in Figure 1.3.

In a PEM fuel cell, hydrogen gas mixed with water stream is supplied at the anode side and air/water stream at the cathode side through the gas flow channels (GFCs). The hydrogen is oxidized in the anode catalyst layer (CL) to release electrons and produce protons. Then, electrons flow through the anode gas diffusion layer (GDL), bi-polar plate (BPP), external circuit and further to the cathode CL. The produced protons are transported through the solid membrane to the cathode side. Oxygen is reduced, meaning that it gains electrons, in the cathode CL and, then, combined with the electrons and protons to produce water and heat. Reactions at the anode and cathode sides, respectively, are given by



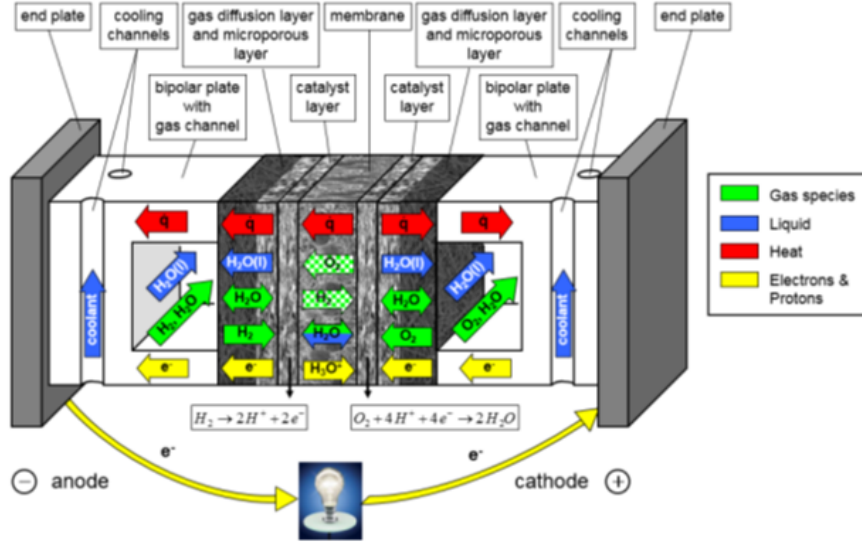


Figure 1.3: Schematic of the transport processes and components in a PEM fuel cell.

The assembled component consisting of the two layers, gas diffusion and catalyst, and a sandwiched membrane is named membrane electrode assembly (MEA). The electrochemical reactions in the cathode attract more attention than the ones in the anode. This is due to the fact that the formation of liquid water at the cathode, especially at high loads, is an issue to be managed in PEM fuel cells. This phenomenon is called flooding and has a negative effect on mass transfer. To avoid flooding at high current densities, the GDLs are usually treated with polytetrafluoroethylene (PTFE). This affects the hydrophobicity of the GDL, leading to the water droplets being forced towards the gas channel [5].

Placing a micro-porous layer (MPL), approximately 30~40 μm , between the gas diffusion layer and catalyst layer is another method of improving the PEM fuel cell performance. The placement of an MPL improves the GDL's liquid water management capability, protects the membrane from punching fibers and is also beneficial in terms of electric and thermal contact of the CL [6].

Porous regions are a main characteristic of a PEM fuel cell as the GDL and CL are porous. These regions consist of pores and a solid matrix. The pores ensure transport of reactants and liquid water through the components while the solid matrix is essential for electrical and heat transport. Regarding the gas diffusion layer, ideally, it provides a uniform distribution of the reactants to the catalyst layer, ensures proper and rapid transport of product electrons to the external circuit and removes liquid water and heat from the catalyst layer [7].

The GDL is made of either carbon fiber paper or carbon cloth. Both types have heterogeneous structures with pore sizes ranging from a few microns to tens of microns. Table 1.1 shows the carbon fiber gas diffusion layer's and catalyst layer's physical properties. The carbon fiber GDL is 0.2~0.5 mm in thickness [8], pores' size is

20~50 μm [9] and the carbon fiber diameter is 5~15 μm [8]. The CL has much smaller pore size than the GDL, this being another reason for applying an micro porous layer between them.

Parameters	GDL	CL
Thickness(mm)	0.2~0.5 [8]	~0.01 [8]
Pore size (μm)	20~50 [9]	0.04~1.0 [10]
Fiber diameter (μm)	5~15 [8]	—
Porosity	0.7~0.8 [9]	0.4~0.6 [11]

Table 1.1: *Physical properties of carbon fiber GDL and CL*

Currently, the automotive industry is considering innovative ways of controlling the porosity distribution of the GDL. However, the cost of fabricating and testing a PEM fuel cell with a complex GDL is considerably high. Moreover, it would be ineffective to proceed with research on these technologies if the gain in the performance that can be achieved with complex porosity distributions of the GDL is minimal. For this reason, computational fluid dynamics (CFD) modeling and simulation can be used to rapidly gain important insight into the working processes inside a GDL with complex porosity. Numerical optimization using CFD models can, then, provide insight into the expected gain in the PEM fuel cell performance.

1.4 Literature Survey

In the past two decades, considerable progress has been achieved in the research focusing on PEM fuel cells and the GDL. The latest achievements greatly contributed to better understanding of the phenomena that take place inside the PEM fuel cell and the GDL as well as to proposing new methodologies for their modeling and optimization. In this section, the literature review of the different approaches to PEM fuel cell and GDL modeling and optimization are presented. The ultimate goal of the literature review that was carried out was, on one hand, to gain insight into the different approaches to modeling and optimizing the PEM fuel cell and GDL and, on the other hand, to find a reliable and suitable software toolbox to serve as the basis model for the subsequent work of this thesis.

Firstly, the different approaches to model the two-phase flow inside the PEM fuel cell/GDL are discussed. From there on, various studies related to the specific topics studied in this thesis are presented and discussed.

1.4.1 On Two-Phase Flow Modeling in GDLs

In PEM fuel cells, two-phase flow originates from the formation of liquid water by the oxygen reduction reaction and the phase change process. The gas phase has multi-components (hydrogen, oxygen, nitrogen and water vapour) while the liquid phase consists only of water. The formation of liquid water, as previously discussed, is an issue to be managed as it can lead to the phenomenon of flooding with negative results on the performance of the PEM fuel cell.

Kone [12] reviews the different approaches to two-phase flow modeling inside the PEM fuel cell. Most commonly in literature, the multi-fluid and the multiphase mixture models are used [17] [23] [27]. However, the Volume of Fluid (VoF) model as well as some more simplified models such as the moisture diffusion and the porosity correction model are also in use [18] [19]. The main water phase change mechanisms used in these models are condensation of water vapour to liquid water and evaporation of liquid water to water vapour.

In the **multi-fluid** model [13] of the two-phase flow, a different set of mass and momentum equations is solved for each phase separately. Usually, the two phases are coupled through the relative permeability and the phase change terms. The use of the multi-fluid model is favorable in high saturation conditions, meaning higher liquid water content in the fuel cell. In these cases the liquid resolution demanded is higher. It can also resolve complex liquid motion and accounts for the convection of liquid by the gas. As far as the disadvantages are concerned, it introduces a high number of variables and the coupling of the phases can be unstable.

In the **multiphase mixture** model [14], the phases are considered to be mixed and a single set of mass and momentum equations are solved for the mixture. This assumes phase equilibrium between the two phases and the mixture variables are evaluated subsequently. The model is best used when the gas pressure is the dominant one and in high capillary pressure values. The model reduces the number of variables and can model the effect of gas pressure on the liquid, but it can be unstable at higher liquid water saturation values.

The **moisture diffusion** model [13] determines the transport of liquid water when the only driving force is the capillary pressure. It solves one more equation for the liquid water transport in which a diffusivity of the liquid water term and a source term due to the phase change of the water are introduced. The moisture diffusion model performs best in low capillary pressure values and when surface tension is the dominant force on the liquid. Also, it only introduces one additional equation. However, the model does not account for the effect of the gas pressure on the liquid.

The **porosity correction** model [13] is the most simplified one as it does not account for the motion of the liquid water. It assumes that liquid water fully occupies some pores of the porous medium. Thus, the porosity at each point is corrected via a function of the liquid water saturation. This approach is best used in very low

relative humidity, very small pore sizes and low loads of the PEM fuel cell and it does not require any additional equations. However, its major drawback is the severe simplification of the phenomenon.

The **VoF** model [15] may locate the interface of gas and liquid in the two-phase flow and advecting the reconstructed interface in a given velocity field. A single momentum equation is solved and the volume fraction of the two phases is tracked throughout the domain. The VoF model is well suited for micro-channel flows where surface tension is a dominant force, however it only deals with the interface of the two phases and a separate CFD model using the multi-fluid or multiphase mixture model is needed to compute the two-phase flow.

1.4.2 PEM Fuel Cell/GDL Modeling & Optimization Studies

The use of CFD to model the processes that take place inside the GDL began about 15 years ago. These models were simplistic and were originally developed for the sake of validating them and implementing CFD on GDL numerical analysis. The domain of these models was usually 1-D and higher dimensional analysis was used rarely. Also, the flow was mostly single-phase and in the cases that two-phase flow was used, the corresponding models were simplistic.

To comment on some characteristic publications employing and validating CFD models for the GDL, Sui [16] developed a model for coupled electron and mass transport in the GDL. The model was quite simplified as it was isothermal and 2-D and the flow was single-phase. It was used for a parametric study on the effects of factors such as conductivity, diffusivity and compression on the current density at the GDL/CL interface. The software in which the model was developed was CFD-ACE+.

However, as previously mentioned, two-phase models were also used during this period. [17] presented a slightly modified approach to the multi-fluid approach to two-phase flow modeling. The model was used and validated in both single-domain and multi-domain formulations and it was shown that the multi-domain formulation has clearly more advantages. However, even though the flow model was two-phase, the general model was still simplistic as it was isothermal and 1-D. The software the was used for developing the model was Comsol Multiphysics.

However, developing CFD models for modeling the flow in the PEM fuel cell, and especially in the GDL, is still ongoing today but with the models being more sophisticated. Kone [18] recently developed a non-isothermal, 3-D, two-phase flow model following the moisture diffusion approach, modeling the whole PEM fuel cell in OpenFOAM. The model was developed in order to be compared with an earlier

developed single-phase model. The importance of the concentration constant in the performance of the PEM fuel cell was also shown in this publication.

Regarding studies on optimization of the GDL porosity, there has been significant work in that field too. The work which was carried out [19] [20] [21] [22] [23] provides insight into the optimal values of porosity in the GDL as well as into the advantages of imposing a porosity distribution in the GDL. However, the downside of the above mentioned work is that the porosity distributions that are usually optimized are simple linear ones or in cases the porosity is even constant. This was done because more complex distributions would likely be too complicated to manufacture. However, recent progress in manufacturing technology of the GDL can make it possible to manufacture more complex porosity distributions.

A characteristic example of such a work is that of Zhan [19] who studied the effects of certain linear porosity distributions on the liquid water flux. The porosity was distributed linearly along the thickness of the GDL and the model (developed in Visual Basic) was isothermal, 1-D and following the moisture diffusion approach for the two-phase flow. In this study, it was found that the liquid water flux increases with increase of contact angle and porosity and decrease of the GDL thickness. It was also found that when using an MPL, the liquid water flux increases with increase of the MPL porosity and decrease of the MPL thickness.

Another related work is that of Secanell [20] [21] [22] who used gradient-based optimization to optimize the constant porosity of the cathode and later the anode GDL. The model of this work was developed on code that was later developed to become part of the OpenFCST project. OpenFCST is an open-source mathematical modeling package for PEM fuel cells developed by the Energy Systems Design Laboratory at the University of Alberta. The model was isothermal, 2-D and single-phase. The GDL porosity was optimized to maximize the current density produced at a certain voltage and, later, also maximize the platinum loading of the CL.

Lastly, Huang [23] developed a non-isothermal, 3-D and two-phase flow model following the multi-fluid approach to optimize linear distributions of the GDL porosity. Porosity was distributed along the thickness of the GDL and was optimized for different types of gas flow channels (GFCs). It was also shown that a linear distribution of porosity enhances species transport and current density and decreases losses.

Due to so many phenomena associated with the porous features of the GDL, it would be useful to take also other publications that do not focus solely on optimizing the porosity into account. For example, Wang [24] studied the effects of the GDL compression on transport phenomena and the overall performance of the PEM fuel cell. His model, developed in *OpenFOAM*[®], was non-isothermal, 3-D and the flow was single-phase. In [24], it is shown that the compression of the GDL leads to decreased porosity which is not favorable for the performance. Also, three zones of different porosity distribution were found in the compressed GDL.

Zhou [25] [26] developed a pore size distribution model to relate micro-structural

information to water accumulation. The model was developed in OpenFCST and was non-isothermal, 2-D and the flow was multi-phase following a mixed pore size distribution and moisture diffusion approach. The MPL was also included and it was shown that, in dry conditions, the MPL has little effect on the PEM fuel cell performance while in wet conditions the MPL improves the performance. Also, a partially hydrophilic MPL might be advantageous.

Niu [27] used a stochastic microstructure for modeling the GDL to study the two-phase flow in mixed wettability conditions. The model was isothermal, 3-D, the flow was two-phase with a mixed multiphase mixture approach and VoF approach and it was developed in *OpenFOAM*[®]. It was shown that mixed wettability conditions are closer to experimental data than purely hydrophobic conditions.

Lastly, it would be important to mention the up-to-date methods of modeling and thoroughly recreating the detailed porous geometry of the GDL in simulations. An alternative to CFD would be the Lattice Boltzmann method [28] which is used more extensively in micro-scale simulations. It is highly suitable for taking the pore geometry into account and is very effective in dealing with complex boundary conditions and multi-phase and multi-component flows. A characteristic publication using this method to model the water transport in the GDL would be that of Hao [29]. Occasionally, along with the Lattice Boltzmann method, the X-ray computed tomography method is used. This method can accurately reproduce the pore geometry of a GDL and matches perfectly with the micro-scale approach of the Lattice Boltzmann method. Jinuntuya [30] used this method along with the Lattice Boltzmann method to study the effects of the GDL structure on water transportation.

1.4.3 Model and Software Selection

For the needs of this thesis, an appropriate software for the PEM fuel cell/GDL model had to be selected for further development and expansion. Taking into account the expertise of the PCopt/NTUA in programming in OpenFOAM and the contributions the team has made to it, OpenFOAM is chosen to be the environment for modeling the PEM fuel cell/GDL. Regarding the toolbox selection, it is considered that the toolbox developed by Kone [18] is an appropriate one for serving as a basis and, then, expanded. The model is quite recent, being non-isothermal, 3-D and the flow being two-phase following the moisture diffusion approach. At the same time, the computational cost of the model is considerably low, being able to run a simulation in approximately ten minutes on one CPU using the same geometry, parameters and number of cells as the author. This factor is of high importance as the toolbox is to be used as the evaluation software in optimization and for this reason needs to be as computationally cheap as possible.

1.5 Scope and Structure of the Thesis

This diploma thesis studies the modeling of the multi-physics phenomena that occur inside a PEM fuel cell, focusing more on the GDL/MPL component, and the optimization of the GDL/MPL porosity distribution for maximum performance of the PEM fuel cell. The phenomena taking place in the fuel cell are simulated by a multi-physics CFD model.

The contents of this diploma thesis are outlined as follows :

- **Chapter 2** : The model of the PEM fuel cell/GDL and its equations and geometry are presented. The model is validated and results for a reference case are computed.
- **Chapter 3** : A parametric study on the impact of different constant GDL porosity values is presented and discussed. The model is extended according to the needs of this study and a first manual optimization of the porosity distribution is presented and discussed.
- **Chapter 4** : The model is coupled with an optimization tool and optimal designs are generated and discussed.
- **Chapter 5** : The work is summarized and conclusions are drawn.

Chapter 2

Model Description & Assessment

2.1 Geometry & Domains

The 3-D geometry of the PEM fuel cell used is the same as the one used by Kone [18] as it uses typical values for the dimensions of a PEM fuel cell. It consists of an anode and cathode pair of bi-polar plates (BPPs), seven anode and cathode pairs of gas flow channels (GFCs) accommodated in the bi-polar plates and a membrane electrode assembly (MEA), meaning an anode and cathode pair of gas diffusion layers (GDLs) and catalyst layers (CLs) and the membrane. The micro-porous layer (MPL) in the GDLs is not accounted for. The GFCs have a constant rectangular cross section from inlet to outlet. The cathode and anode are symmetrical. The mesh consists of a total of 134552 cells. The geometry as well as the mesh of the PEM fuel cell are shown in figure 2.1 while figure 2.2 shows the anode and cathode GFCs in detail. Table 2.1 gives the analytical dimensions of each component as well as the number of cells in each direction. The x axis denotes the BPP to BPP direction or the width of the PEM fuel cell, the y axis denotes the channel to channel direction or the height and the z axis denotes the inlet to outlet direction or the length.

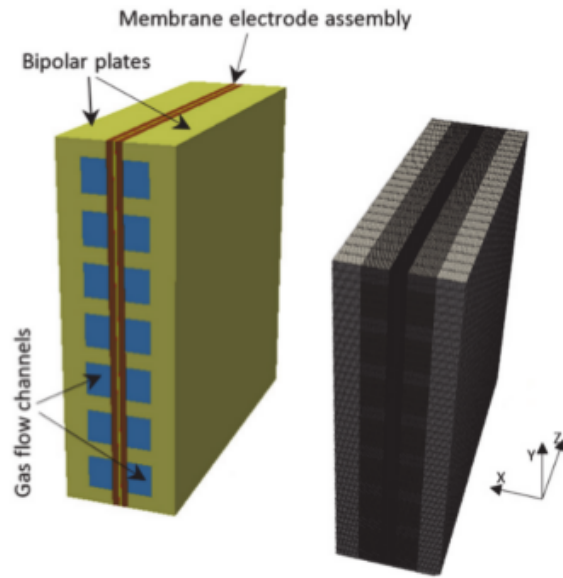


Figure 2.1: *Geometry and mesh of the PEM fuel cell [18].*

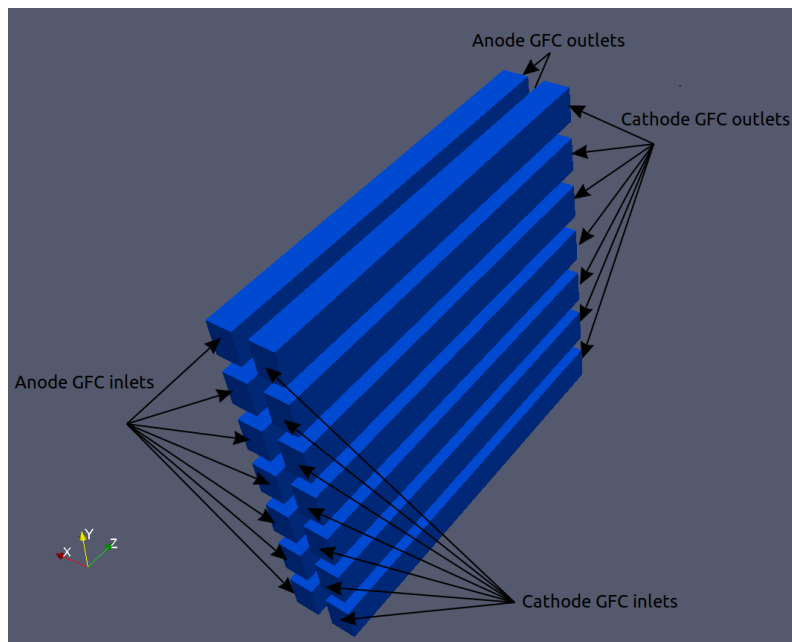
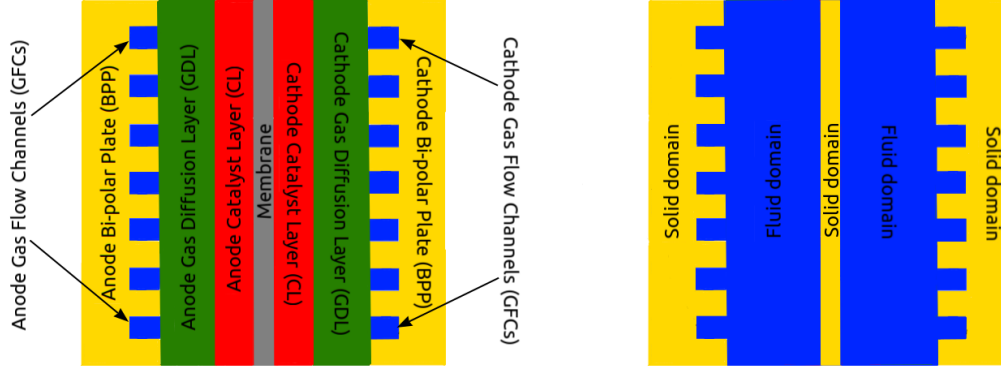


Figure 2.2: *Detailed geometry of anode and cathode gas flow channels.*

	Membrane	CL	GDL	GFC	BPP
Width (mm) / # of cells	0.127 / 5	0.0037 / 2	0.41 / 20	1.5 / 30	3 / 45
Height (mm) / # of cells	22 / 44	22 / 44	22 / 44	2 / 4	22 / 44
Length (mm) / # of cells	22 / 22	22 / 22	22 / 22	22 / 22	22 / 22

Table 2.1: *Dimensions and number of cells of each component of the PEM fuel cell [18].*

Due to the various phenomena that occur, the PEM fuel cell is broken down into two domains where different equations are solved. As shown in the 2D schematics of figure 2.3, the geometry is divided in the fluid domain and the solid domain. The fluid domain consist of the GDL, the CL and the GFCs in the cathode and anode respectively. Despite the fact that in the fluid domain, only the GDL and CL are porous, porosity is applied everywhere in the domain. However, in the GFCs the porosity value is set to 1, meaning that they are completely empty. In the fluid domain the liquid water saturation equation and the mass, momentum, energy and species conservation equations are solved. The solid domain consists of the BPPs and the membrane. There, only the energy equation is solved due to the heat transported from the fluid domains. Lastly, the interface between the cathode fluid domain and the membrane, even though it is not considered a domain in itself, is where the electrochemical phenomena take place and the electrochemical reaction equations are solved. These are coupled with the equations in the fluid domain via the Nernst equation which computes the potential (voltage) produced by the electrochemical reactions.



(a) Schematic of all the components of the PEM fuel cell.

(b) Schematic of the domain partition.

Figure 2.3: Schematics (not in scale) of the components of the fuel cell and the domain partition due to the different equations that need to be solved.

2.2 Assumptions

Before presenting the model equations, the assumptions made have to be presented. These are the following :

- All components are considered homogenous and isotropic
- Reactant gases do not permeate the membrane
- The electrochemical reactions occur at the interface between the membrane and the cathode CL
- Activation and concentration overpotentials are neglected in the anode
- Joule heating is neglected in the BPPs due to high heat conductivity
- In the BPPs, electrical potential distribution is constant due to high electrical conductivity of the material
- The gas flow is steady, laminar and incompressible due to low velocities and steady-state operating conditions
- All gases are treated as perfect

- The outer walls of the entire cell are adiabatic
- The velocity of the liquid is equal to the velocity of the gas inside the GFCs where the two-phases also share the same pressure and temperature
- Water vapour is in equilibrium with liquid water at their interface

2.3 Governing Equations

The governing equations of the model are the conservation of mass, momentum, energy and chemical species, the liquid water transport equation and the cell voltage equation. The conservation of mass, momentum and energy equations constitute the modified Navier-Stokes equations.

The **conservation of mass** concerns the gas mixture, is solved in the fluid domain and is expressed as

$$\nabla \cdot (\rho_g \vec{U}_g) + S_l = 0 \quad (2.1)$$

where ρ_g and \vec{U}_g are the density and velocity of the gas mixture respectively. Even though the flow is incompressible, ρ_g is not constant as it is a function of the mass fractions of each component of the gas mixture. The gas mixture comprises the various reactant gases, O_2 , N_2 and water vapour in the cathode and H_2 and water vapour in the anode. S_l is the mass source term due to the water phase change from gas to liquid expressed as [31]

$$S_l = -C_r \frac{\varepsilon (1 - s) (x_{WV} p_g - p_{sat})}{RT} M_{H_2O} \quad (2.2)$$

where C_r is the condensation rate (Table 2.3), ε is the porosity (Table 2.3), s is the liquid water saturation (Table 2.4), x_{WV} is the water vapour mole fraction, p_g is the pressure of the gas mixture, p_{sat} is the saturation pressure, R is the universal gas constant equal to $8.134 \frac{J}{mol K}$, T is the temperature and M_{H_2O} is the molar mass of H_2O equal to $18.016 \frac{g}{mol}$. Porosity ε is defined as the volume fraction of the void space while liquid water saturation s is defined as the volume fraction of the liquid water.

The **conservation of momentum** concerns the gas mixture, is solved in the fluid domain and is expressed as

$$\nabla \cdot (\rho_g \vec{U}_g \vec{U}_g) = -\nabla p_g + \nabla \cdot (\mu_g \nabla \vec{U}_g) + \vec{S}_M \quad (2.3)$$

where μ_g is the dynamic viscosity of the gas mixture and S_M is the momentum source term which is equal to the Darcy resistance in the porous media and is expressed as

$$\vec{S}_M = -\frac{\mu_g \vec{U}_g}{K_g} \quad (2.4)$$

where K_g is the permeability of the porous medium which is a material property.

The **conservation of chemical species** is solved in the fluid domain and is expressed as

$$\nabla \cdot (\rho_g \vec{U}_g y_i) = \nabla \cdot (\rho_g D_{g,i}^{eff} \nabla y_i) \quad (2.5)$$

where y_i is the mass fraction of species i and $D_{g,i}^{eff}$ is the effective diffusivity of the species i . $D_{g,i}^{eff}$ is correlated with the diffusivity of each gas species $D_{g,i}$ (Table 2.4) via porosity and liquid water saturation by [32]

$$D_{g,i}^{eff} = D_{g,i} \varepsilon \frac{((1-s) - 0.11)^{0.9}}{(1-0.11)^{0.9}} \quad (2.6)$$

The **conservation of energy** is solved in both fluid and solid domains, with different expressions in each of them. In the fluid domain, it is expressed as

$$\nabla \cdot (\rho_{mix} c_{p_{mix}} \vec{U}_g T) = \nabla \cdot (k_{mix} \nabla T) + S_E^{PC} \quad (2.7a)$$

where ρ_{mix} is the density of the gas-liquid mixture, $c_{p_{mix}}$ is the specific heat capacity of the gas-liquid mixture, k_{mix} is the thermal conductivity of the gas-liquid mixture and S_E^{PC} is the source term due to the water phase change.

In the membrane solid domain, the corresponding equation is expressed as

$$\nabla \cdot (k_{MEM} \nabla T) + S_E^{reac} = 0 \quad (2.7b)$$

where k_{MEM} is the thermal conductivity of the solid material of the membrane (Table 2.3) and S_E^{reac} is the source term due to heat released by the reactions.

Finally, in the BPP solid domain, the equation is expressed as

$$\nabla \cdot (k_{BPP} \nabla T) = 0 \quad (2.7c)$$

where k_{BPP} is the thermal conductivity of the solid material of the BPP (Table 2.3).

S_E^{reac} and S_E^{PC} are expressed as

$$S_E^{reac} = \frac{I}{\delta_{MEA}} \left(\eta - \frac{T \left(\sum \frac{S_{i,prod}}{n_i} - \sum \frac{S_{i,react}}{n_i} \right)}{F} \right) \quad (2.8)$$

$$S_E^{PC} = S_l h_{mfg} \quad (2.9)$$

where I is the current density produced by the electrons' flow (Table 2.4), δ_{MEA} is the thickness of the MEA, η is the total overpotential (voltage loss), $S_{i,prod}$ and $S_{i,react}$ is the entropy of each produced and reactant species respectively (Table 2.3), n_i is the number of electrons of species i , F is Faraday's constant equal to $96485 \frac{C}{mol}$ and h_{mfg} is the specific latent heat of evaporation or condensation of water which is measured in $\frac{J}{mol}$ and empirically determined by [33]

$$h_{mfg} = 45070 - 41.9(T - 273.15) + 3.44 \cdot 10^{-3}(T - 273.15)^2 + 2.54 \cdot 10^{-6}(T - 273.15)^3 - 8.98 \cdot 10^{-10}(T - 273.15)^4 \quad (2.10)$$

Figure 2.4 gives the graph of h_{mfg} as a function of T for a range of T between 273.15-500 Kelvin.

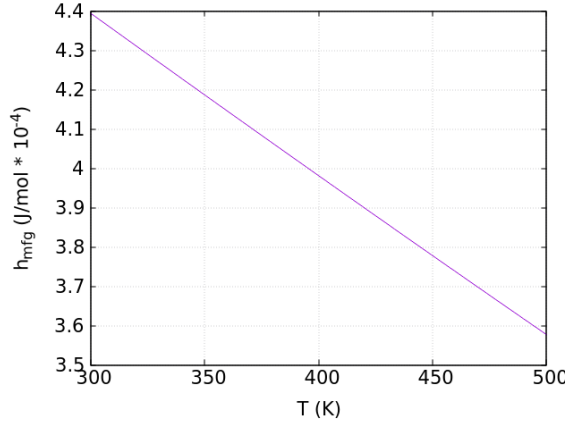


Figure 2.4: Specific latent heat of evaporation or condensation of water h_{mfg} as a function of temperature T (plot corresponding to eq. 2.10)

The **liquid water transport equation** is solved in the fluid domain and reads [31]

$$\nabla \cdot (\rho_l D_l \nabla s) - \nabla \cdot (\rho_g \vec{U}_g s) + S_l = 0 \quad (2.11)$$

where ρ_l is the density of the liquid water and D_l is the diffusivity of the liquid water expressed as

$$D_l = \frac{K_l \partial p_c}{\mu_l \partial s} \quad (2.12)$$

where K_l is the permeability of the liquid water, μ_l is the dynamic viscosity of the liquid water and p_c is the capillary pressure.

Lastly, the **cell voltage output** is computed in the cathode fluid/solid domain interface and is expressed as

$$V_{cell} = E_{Nernst} - \eta_{act} - \eta_{ohm} - \eta_{con} \quad (2.13)$$

where E_{Nernst} is the Nernst potential and η_{act} , η_{ohm} and η_{con} are the activation, ohmic and concentration overpotentials, respectively. E_{Nernst} , η_{act} , η_{ohm} and η_{con} are all field variables and subsequently V_{cell} is a field variable. To produce a single value for the voltage output, V_{cell} is averaged in the fluid/solid domain interface.

2.4 Constitutive Equations

Regarding the constitutive equations of the model, firstly, the molar fraction x_i is related to the mass fraction y_i by

$$x_i = \frac{y_i}{M_i \sum \frac{y_j}{M_j}} \quad (2.14)$$

The local open-circuit potential produced by the electrochemical reaction is given by the Nernst equation

$$E_{Nernst} = E_0 + \frac{RT}{zF} \ln Q \quad (2.15)$$

where E_{Nernst} is the cell potential, z is the number of electrons transferred which equals 2, Q is the reaction quotient and E_0 is the standard cell potential expressed as

$$E_0 = -\Delta G = -(\Delta H - T\Delta S) \quad (2.16)$$

where ΔG is the Gibbs free energy, ΔH is the enthalpy of formation of the reaction products and ΔS is the entropy of formation of the reaction products.

The cell activation overpotential is expressed as [34]

$$\eta_{act} = \frac{RT}{\alpha F} \ln \left(\frac{I}{I_{0c}} \right) \quad (2.17)$$

where α is the charge transfer coefficient (Table 2.3) and I_{0c} is the exchange current density at the cathode measured also in $\frac{A}{m^2}$ and given by [35]

$$I_{0c} = I_0^{ref} \exp \left[\frac{-E_{act}}{R} \left(\frac{1}{T} - \frac{1}{353.15} \right) \right] \quad (2.18)$$

where I_0^{ref} is the reference exchange current density (Table 2.3) and E_{act} is the activation energy (Table 2.3).

The cell ohmic overpotential is expressed as [34]

$$\eta_{ohm} = R_{\Omega} I \quad (2.19)$$

where R_{Ω} is the area specific resistance of the cell defined by

$$R_{\Omega} = \int_0^{\delta_{MEM}} \frac{dx}{\sigma_i} + \frac{\delta_{CGDL}}{\sigma_{eCGDL}^{eff}} + \frac{\delta_{CCL}}{\sigma_{eCCL}^{eff}} + \frac{\delta_{AGDL}}{\sigma_{eAGDL}^{eff}} + \frac{\delta_{ACL}}{\sigma_{eACL}^{eff}} + \frac{\delta_{BPPs}}{\sigma_{eBPPs}} + R_C \quad (2.20)$$

where MEM , $CGDL$, CCL , $AGDL$, ACL , $BPPs$ denote the membrane, cathode GDL, cathode CL, anode GDL, anode CL and BPPs respectively, δ is thickness, R_C is the contact resistance between the BPP and GDL (Table 2.3), σ_e^{eff} is the effective electrical conductivity calculated as

$$\sigma_e^{eff} = \sigma_e (1 - \varepsilon) \quad (2.21)$$

σ_i is the ionic conductivity written as [37]

$$\sigma_i = (0.5139\lambda - 0.326) \exp \left[1268 \left(\frac{1}{303} - \frac{1}{T} \right) \right] \quad (2.22)$$

where λ is the dimensionless membrane water content defined as [37]

$$\lambda = \begin{cases} 0.043 + 17.18a - 39.85a^2 + 36a^3, & 0 < a < 1 \\ 14 + 1.4(a - 1), & 1 \leq a \leq 3 \end{cases} \quad (2.23)$$

with a being the activity of water vapour in the gas mixture calculated as [37]

$$a = \frac{x_{WV} p_g}{p_{sat}} \quad (2.24)$$

Lastly, p_{sat} measured in *atm* is given by [37]

$$\log p_{sat} = -2.1794 + 0.02953(T - 273.15) - 9.1837 \cdot 10^{-5}(T - 273.15)^2 + 1.4454 \cdot 10^{-7}(T - 273.15)^3 \quad (2.25)$$

Figure 2.5 shows the graph of the dimensionless membrane water content λ as a function of the activity of water vapour in the gas mixture a . Figure 2.6 shows the graph of the saturation pressure p_{sat} as a function of the temperature T .

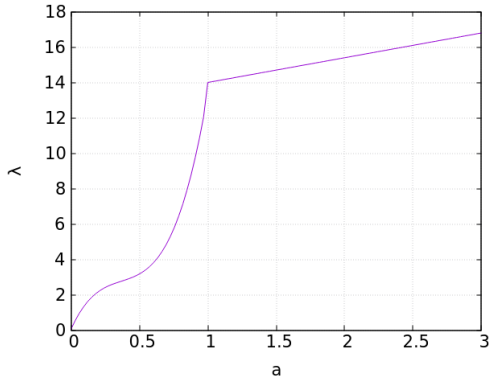


Figure 2.5: Dimensionless membrane water content λ as a function of the activity of water vapour in the gas mixture a (plot corresponding to eq. 2.23).

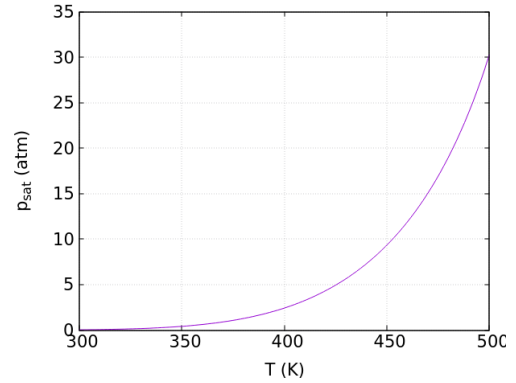


Figure 2.6: Saturation pressure p_{sat} as a function of the temperature T (plot corresponding to eq. 2.25).

The concentration overpotential is expressed as [36]

$$\eta_{con} = c \ln \left(\frac{I_{Lc}}{I_{Lc} - I} \right) \quad (2.26)$$

where c is the concentration constant (Table 2.3) and I_{Lc} is the cathode limiting current density expressed as [36]

$$I_{Lc} = \frac{n_{O_2} F D_{O_2} C_{O_2}}{\delta_{CGDL}} \quad (2.27)$$

where n_{O_2} is the number of electrons exchanged by oxygen which equals 4, D_{O_2} is the diffusivity of oxygen (Table 2.4), C_{O_2} is the concentration of oxygen and δ_{CGDL} is the thickness of the cathode GDL.

The capillary pressure of liquid water in the porous media is expressed as [35]

$$p_c = \sigma \cos\theta \left(\frac{\varepsilon}{K} \right)^{\frac{1}{2}} J(s) \quad (2.28)$$

where σ is the surface tension (Table 2.3), θ is the liquid water contact angle (Table 2.3) and $J(s)$ is the Leverett function defined as [35]

$$J(s) = 1.417(1 - s) - 2.12(1 - s)^2 + 1.263(1 - s)^3 \quad (2.29)$$

Figure 2.7 shows how the contact angle of a liquid water droplet is defined and figure 2.8 gives the Leverett function graph.

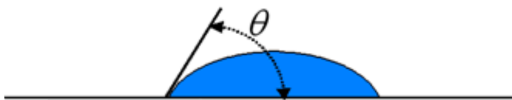


Figure 2.7: *Liquid water droplet contact angle measurement.*

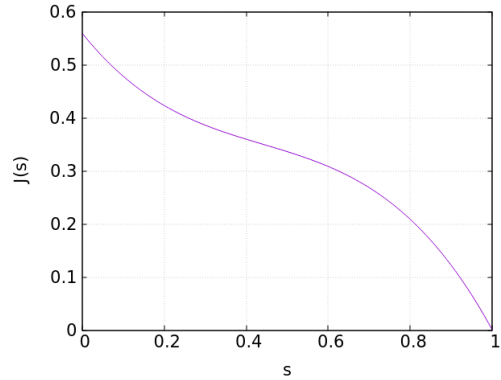


Figure 2.8: *Leverett function graph with respect to liquid water saturation s*

The density of the two-phase mixture ρ_{mix} is defined by

$$\rho_{mix} = (1 - s)\rho_g + s\rho_l \quad (2.30)$$

The specific heat capacity of the two-phase mixture $c_{p_{mix}}$ is defined by

$$c_{p_{mix}} = (1 - s)c_{p_g} + sc_{p_l} \quad (2.31)$$

The thermal conductivity of the two-phase mixture k_{mix} is defined by

$$k_{mix} = (1 - s)k_g + sk_l \quad (2.32)$$

2.5 Boundary Conditions

The boundaries of the computational domains consist of the outer wall boundaries, the gas flow channels' inlets and outlets and the various interfaces between fluid and solid domains. Figure 2.9 shows a 2D schematic of the outer wall boundaries as well as the various interfaces. Table 2.2 contains the specific boundary values for the reference case at $I = 0.6 \frac{A}{cm^2}$ which is to be used in the work to follow in this chapter.

At the GFCs' inlets, Dirichlet conditions are applied for velocity, temperature, liquid water saturation and species mass fractions while Neumann conditions are applied to pressure. The inlet velocity is a function of the species stoichiometric flow ratio ξ , the current density I , the electrode active area A_{MEA} and the GFC cross section area A_{ch} and is calculated as

$$U_{in} = \xi \frac{I}{nF} A_{MEA} \frac{1}{x_i} \frac{RT}{p} \frac{1}{A_{ch}} \quad (2.33)$$

At the GFCs' outlets, Dirichlet conditions are imposed on pressure while Neumann conditions on velocity, temperature, liquid water saturation and species mass fractions.

At the solid domain - outer wall boundaries, zero Neumann conditions of temperature are imposed. At the fluid domain - outer wall boundaries, as well as in all the fluid - solid interfaces, zero Neumann conditions are imposed on temperature, pressure, liquid water saturation and species mass fractions and zero Dirichlet conditions on velocity.

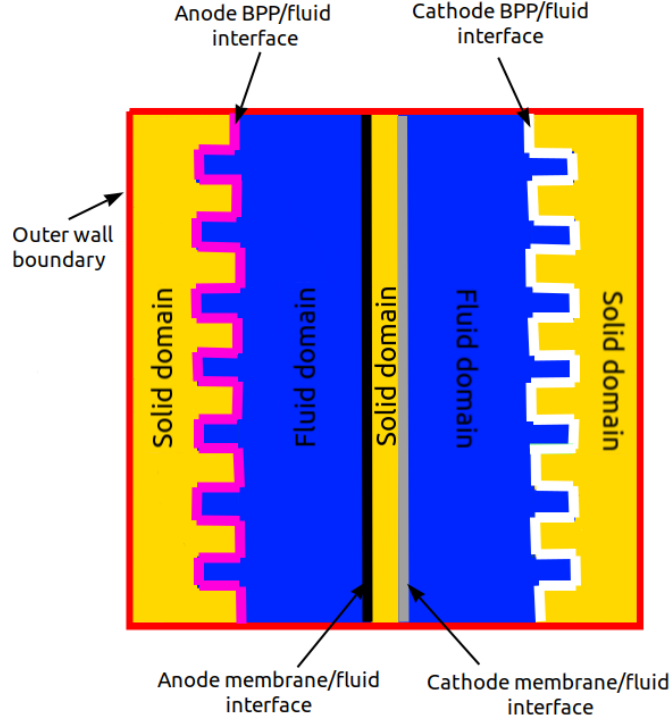


Figure 2.9: 2D schematic of computational domain's outer wall and interface boundaries.

Anode Inlet	Anode Outlet	Cathode Inlet	Cathode Outlet	Fluid - Solid & Fluid - Outer Wall	Solid - Outer Wall
$U_{fuel} = 0.8844 \frac{m}{s}$	$\nabla_n U_{fuel} = 0$	$U_{air} = 2.4656 \frac{m}{s}$	$\nabla_n U_{air} = 0$	$U = 0$	
$\nabla_n p_{fuel} = 0$	$p_{fuel} = 101325 Pa$	$\nabla_n p_{air} = 0$	$p_{air} = 101325 Pa$	$\nabla_n p = 0$	
$y_{H_2} = 0.2$	$\nabla_n y_{H_2} = 0$	$y_{O_2} = 0.2$	$\nabla_n y_{O_2} = 0$	$\nabla_n y = 0$	
$y_{H_2O} = 0.8$	$\nabla_n y_{H_2O} = 0$	$y_{H_2O} = 0.15$	$\nabla_n y_{H_2O} = 0$		
		$y_{N_2} = 0.65$	$\nabla_n y_{N_2} = 0$		
$T = 353K$	$\nabla_n T = 0$	$T = 353K$	$\nabla_n T = 0$	$\nabla_n T = 0$	$\nabla_n T = 0$
$s = 0.2$	$\nabla_n s = 0$	$s = 0.2$	$\nabla_n s = 0$	$\nabla_n s = 0$	

Table 2.2: Reference case boundary condition values.

2.6 Reference Case Parameters Values & Operating Conditions

The reference case parameters and operating conditions are the same as those used in [18]. Table 2.3 displays the values of the various parameters needed for solving

the model. Table 2.4 contains the values of the PEM fuel cell operating condition parameters at the reference case.

Table 2.3: *Parameter values*

Parameter (Units)	Symbol	Value
Density of air ($\frac{kg}{m^3}$)	ρ_{air}	0.914
Density of fuel ($\frac{kg}{m^3}$)	ρ_{fuel}	0.2404
Density of liquid water ($\frac{kg}{m^3}$)	ρ_l	1000
Density of membrane ($\frac{kg}{m^3}$)	ρ_{MEM}	1980
Density of BPP ($\frac{kg}{m^3}$)	ρ_{BPP}	1880
Heat capacity of air ($\frac{J}{kgK}$)	$c_{p_{air}}$	1108.85
Heat capacity of fuel ($\frac{J}{kgK}$)	$c_{p_{fuel}}$	2062.74
Heat capacity of liquid water ($\frac{J}{kgK}$)	c_{p_l}	4190
Heat capacity of GDL ($\frac{J}{kgK}$)	$c_{p_{GDL}}$	710
Heat capacity of CL ($\frac{J}{kgK}$)	$c_{p_{CL}}$	710
Heat capacity of membrane ($\frac{J}{kgK}$)	$c_{p_{MEM}}$	2000
Heat capacity of BPP ($\frac{J}{kgK}$)	$c_{p_{BPP}}$	875
Thermal conductivity of air ($\frac{W}{mK}$)	k_{air}	0.02867
Thermal conductivity of fuel ($\frac{W}{mK}$)	k_{fuel}	0.08396
Thermal conductivity of liquid water ($\frac{W}{mK}$)	k_l	0.6
Thermal conductivity of GDL ($\frac{W}{mK}$)	k_{GDL}	1.6
Thermal conductivity of CL ($\frac{W}{mK}$)	k_{CL}	8
Thermal conductivity of membrane ($\frac{W}{mK}$)	k_{MEM}	0.67
Thermal conductivity of BPP ($\frac{W}{mK}$)	k_{BPP}	10.7
Electronic conductivity of GDL ($\frac{S}{m}$)	$\sigma_{e_{GDL}}$	5000
Electronic conductivity of CL ($\frac{S}{m}$)	$\sigma_{e_{CL}}$	1000
Electronic conductivity of BPP ($\frac{S}{m}$)	$\sigma_{e_{BPP}}$	83000
Dynamic viscosity of air ($Pa\ s$)	μ_{air}	1.5158×10^{-5}
Dynamic viscosity of fuel ($Pa\ s$)	μ_{fuel}	1.5×10^{-5}
Porosity of GDL	ε_{GDL}	0.5
Porosity of CL	ε_{CL}	0.4
Contact resistance (Ωm^2)	R_C	2×10^{-6}
Cathode charge transfer coefficient	α_c	1.0
Cathode activation energy ($\frac{J}{mol}$)	E_{act_c}	73220
Reference exchange current density ($\frac{A}{m^2}$)	I_0^{ref}	0.0139
Concentration constant	c	0.25
Condensation rate ($\frac{1}{s}$)	C_r	10
Surface tension ($\frac{N}{m}$)	σ	0.0625
Liquid water contact angle ($^\circ$)	θ	120
Enthalpy of formation of water vapour ($\frac{J}{mol}$)	ΔH_{H_2O}	-241826

Table 2.3: *Parameter values*

Parameter (Units)	Symbol	Value
Standard entropy of hydrogen ($\frac{J}{molK}$)	S_{H_2}	130.68
Standard entropy of oxygen ($\frac{J}{molK}$)	S_{O_2}	205.152
Standard entropy of nitrogen ($\frac{J}{molK}$)	S_{N_2}	191.609
Standard entropy of water vapour ($\frac{J}{molK}$)	S_{H_2O}	188.835

Table 2.4: *Reference case PEM fuel cell operating conditions*

Parameter (Units)	Symbol	Value
Cell current density ($\frac{A}{cm^2}$)	I	0.6
Cell temperature (K)	T_{cell}	353
Cathode fluid pressure (Pa)	p_{ca}	101325
Anode fluid pressure (Pa)	p_{an}	101325
Cathode fluid velocity ($\frac{m}{s}$)	U_{ca}	2.4656
Anode fluid velocity ($\frac{m}{s}$)	U_{an}	0.8844
O_2 diffusivity in air mixture ($\frac{m^2}{s}$)	$D_{O_2,air}$	2.939×10^{-5}
Effective O_2 diffusivity in GDL ($\frac{m^2}{s}$)	$D_{O_2,GDL}^{eff}$	9.732×10^{-6}
Effective O_2 diffusivity in CL ($\frac{m^2}{s}$)	$D_{O_2,CL}^{eff}$	7.785×10^{-6}
H_2 diffusivity in fuel mixture ($\frac{m^2}{s}$)	$D_{H_2,fuel}$	1.22×10^{-4}
Effective H_2 diffusivity in GDL ($\frac{m^2}{s}$)	$D_{H_2,GDL}^{eff}$	4.031×10^{-5}
Effective H_2 diffusivity in CL ($\frac{m^2}{s}$)	$D_{H_2,CL}^{eff}$	1.252×10^{-5}
Anode liquid water saturation	s	0.2
Cathode liquid water saturation	s	0.2
O_2 mass fraction	y_{O_2}	0.2
H_2O air mass fraction	y_{H_2O}	0.15
N_2 mass fraction	y_{N_2}	0.65
H_2 mass fraction	y_{H_2}	0.2
H_2O fuel mass fraction	y_{H_2O}	0.8
Stoichiometry ratio in cathode air	ξ_{air}	2
Stoichiometry ratio in anode fuel	ξ_{fuel}	1.5

2.7 I-V Curve & Overpotentials

By keeping all the reference case parameters constant, varying the current density up to $1.6 \frac{A}{cm^2}$ and running the simulations, the I-V curve is produced. Figure 2.10 shows this I-V curve. The curve follows the typical trend and behaves as expected,

with the cell voltage output decreasing as the current density or load of the PEM fuel cell decreases.

Figure 2.11 displays the overpotentials or potential losses for the varying current densities. The activation overpotential constitutes the largest potential loss at any current density because of slow reaction rates at the electrodes. The ohmic potential loss becomes significant at moderate current densities due to resistance to the flow of electrons and protons. The concentration overpotential, caused by mass transport, rises at high current densities as the electrodes are rapidly depleted of the reactants by the electrochemical reactions.

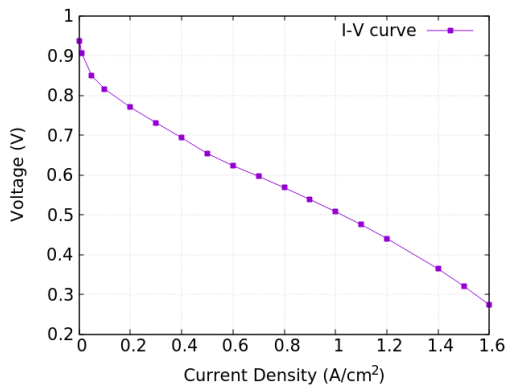


Figure 2.10: *I-V curve in reference case parameters and varying current density.*

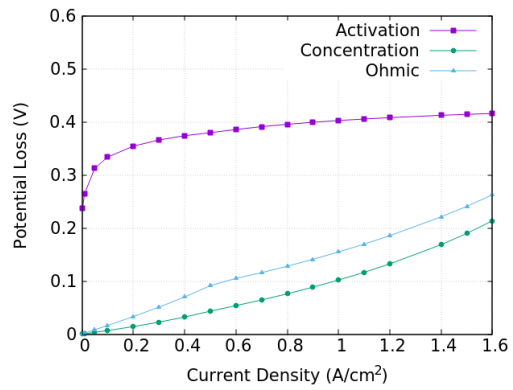


Figure 2.11: *Overpotentials in reference case parameters and varying current density.*

2.8 Discussion on the Reference Case Results

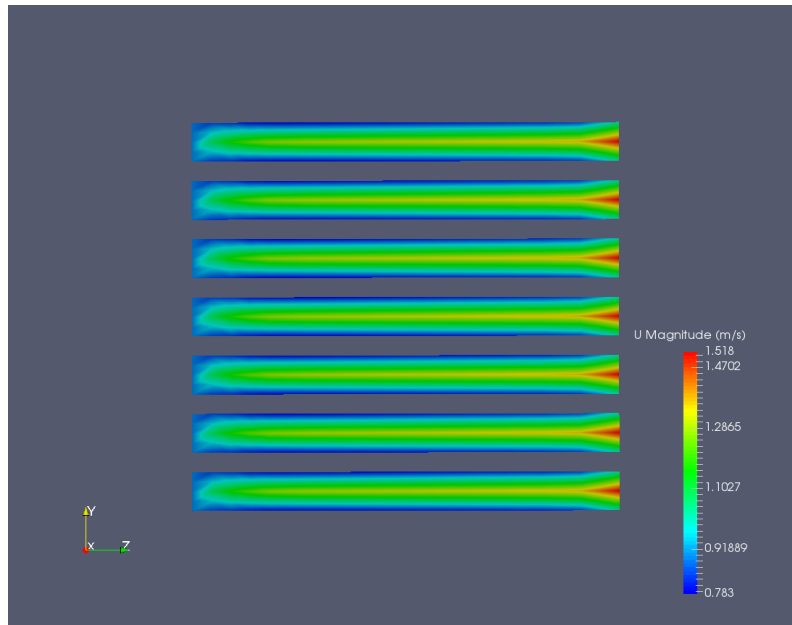
The post-processing and visualization of the reference case results were achieved with ParaView, an open-source post-processing utility used with OpenFOAM.

2.8.1 Gas Flow Channels Results

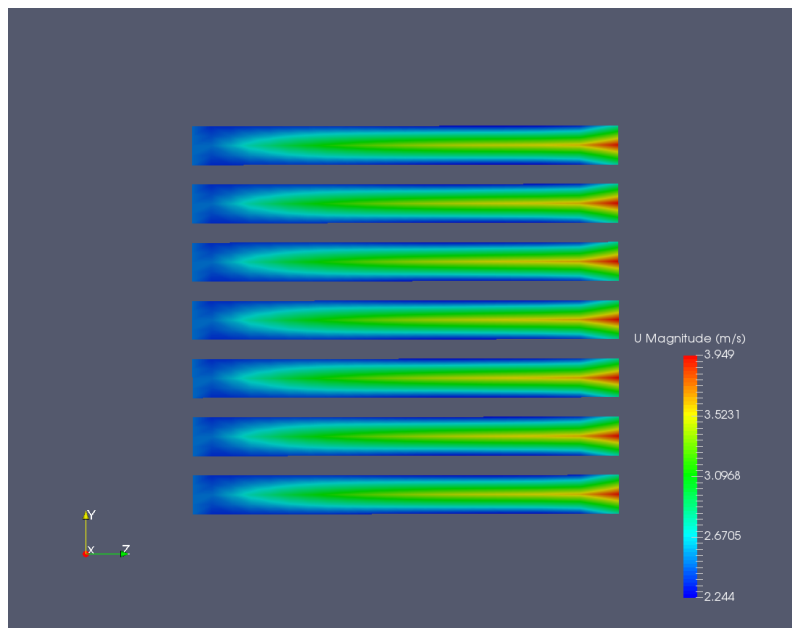
Figure 2.12 displays the velocity profiles along the anode and cathode gas flow channels (GFCs), for fuel and air respectively, on the slice midway between the BPP and GDL. Note that the inlet is on the left of the figures while the outlet is at the right. The highest velocity is observed at the center lines of the channels at the cell outlet while the lowest velocity is seen at the walls. These profiles agree with fully developed laminar flows.

In the same slice, figure 2.13 illustrates the pressure profiles for the anode fuel and cathode air. The increase in the fluid velocity from inlet to outlet results in a decrease in the fluid pressure. However, the pressure drops along the channels are rather small, around 1 Pa in the anode and 8 Pa in the cathode.

Figure 2.14 shows the distribution of hydrogen and oxygen mass fractions at the anode and cathode GFC, respectively. As the reactants are consumed during the electrochemical reactions, their mass fractions decrease from the cell inlet to the cell outlet. It can also be seen that the concentration of reactant gases is proportional to pressure.

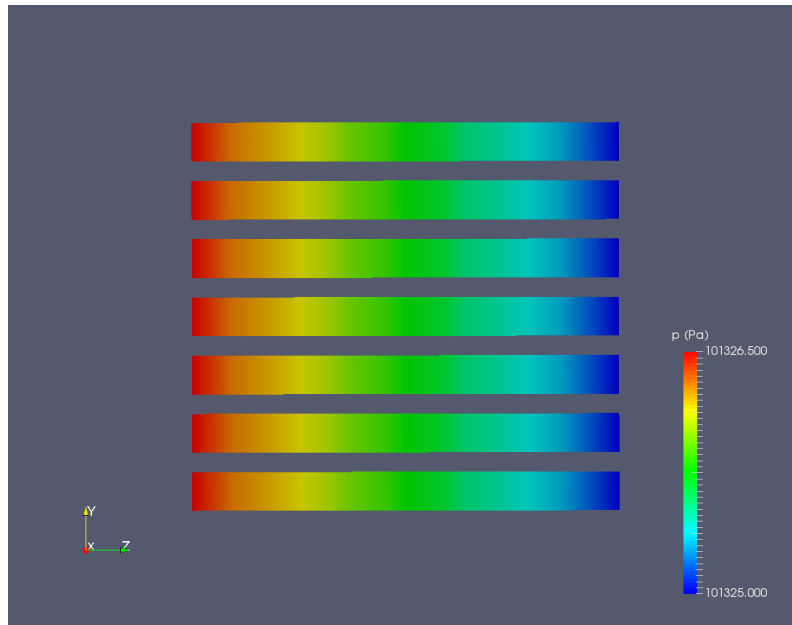


(a) Anode GFC velocity magnitude

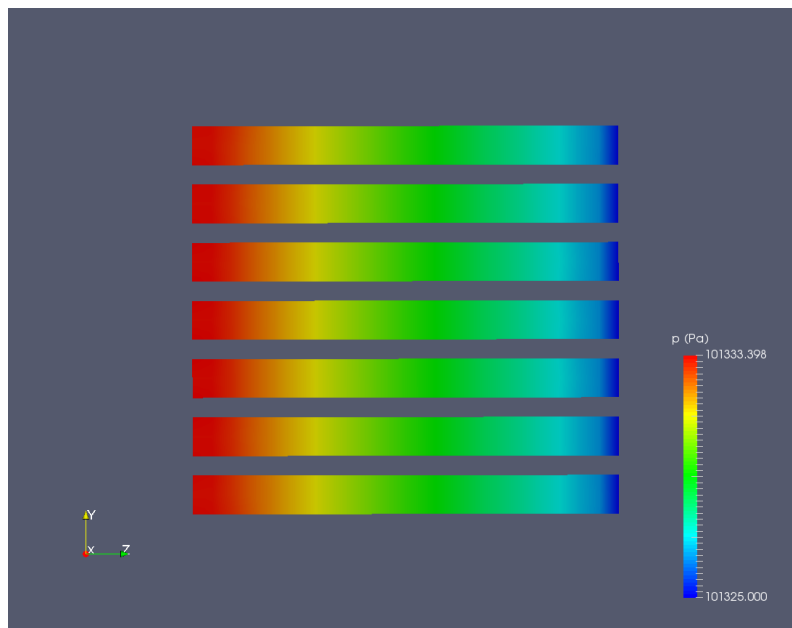


(b) Cathode GFC velocity magnitude

Figure 2.12: Reference case anode and cathode GFC velocity magnitude profile midway between BPP and GDL

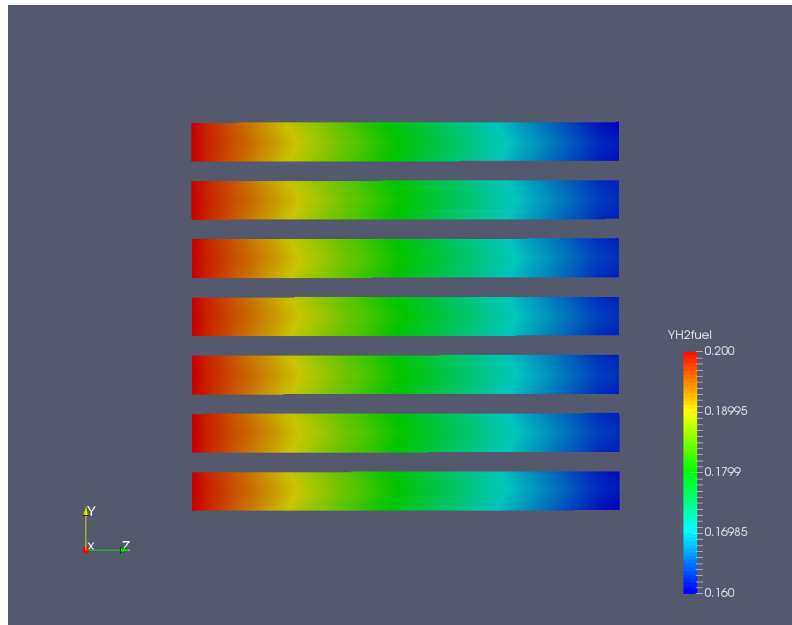


(a) Anode GFC pressure

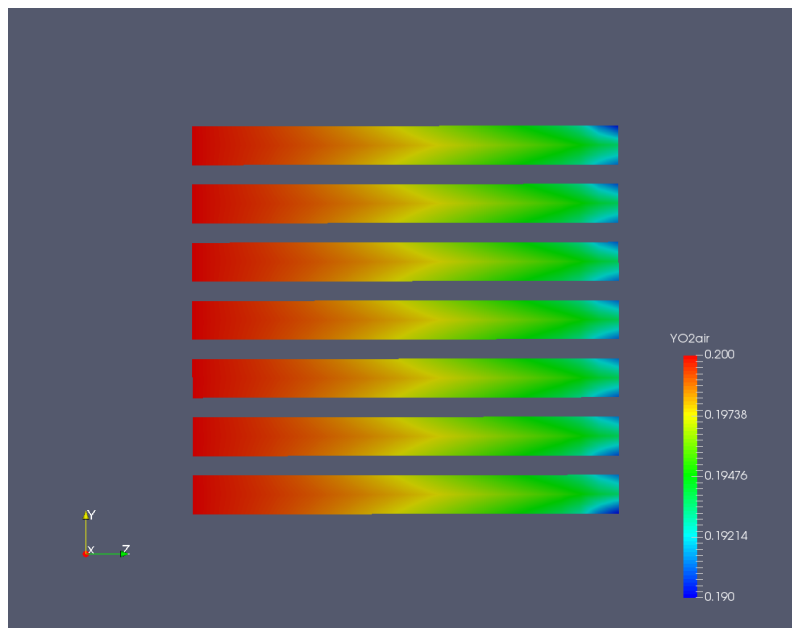


(b) Cathode GFC pressure

Figure 2.13: Reference case anode and cathode GFC pressure profile midway between BPP and GDL



(a) Anode GFC hydrogen mass fraction



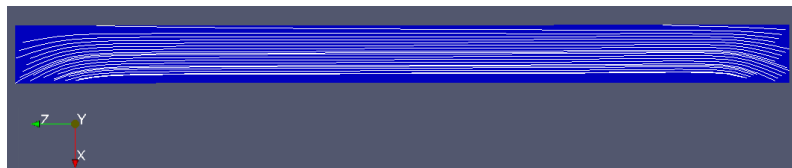
(b) Cathode GFC oxygen mass fraction

Figure 2.14: Reference case anode and cathode GFC hydrogen and oxygen mass fraction profiles midway between BPP and GDL

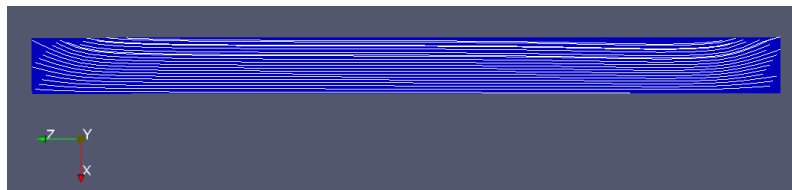
2.8.2 Gas Diffusion Layer Results

Figure 2.16 shows the velocity profiles in the cathode and anode gas diffusion layer (GDL), in a slice mid-height of the whole PEM fuel cell, essentially where the centerline of the middle channel is. The inlet is on the right of the figure while the outlet on the left. For the cathode, the BPP would be above the image while the CL would be below and vice-versa for the anode. Moreover, figure 2.15 shows the stream lines of the flow on that same slice. For both the anode and the cathode, it can be observed that the flow goes almost parallel from the inlet to outlet with the flux to the CL being very small compared to the total flow. Also, the flow enters the GDL very close to the inlet and exits the GDL very close to the outlet, meaning that the reactants are not evenly distributed to the CL.

Figure 2.17 displays the velocity profiles in the cathode and anode GDL, in a slice mid-length of the PEM fuel cell from inlet to outlet. It can be seen from this figure that the velocity profiles repeat from the channel to channel, meaning that figure 2.16 is representative of all the channels. It can also be observed that the flow from channel to channel is present but small.

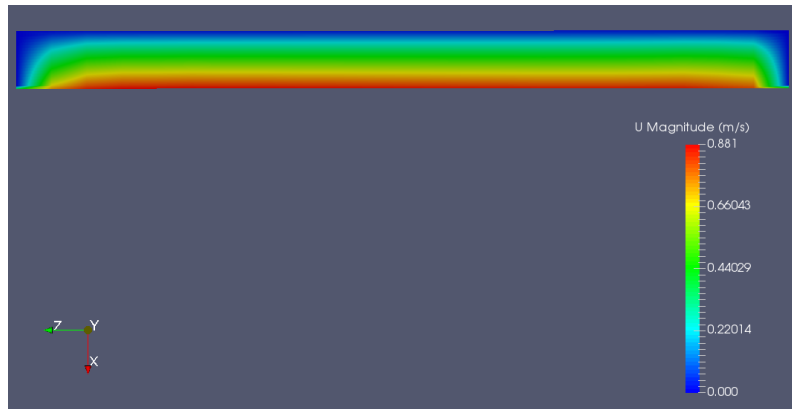


(a) *Anode GDL flow stream lines mid-height*



(b) *Cathode GDL flow stream lines mid-height*

Figure 2.15: *Reference case anode and cathode GDL flow stream lines mid-height*

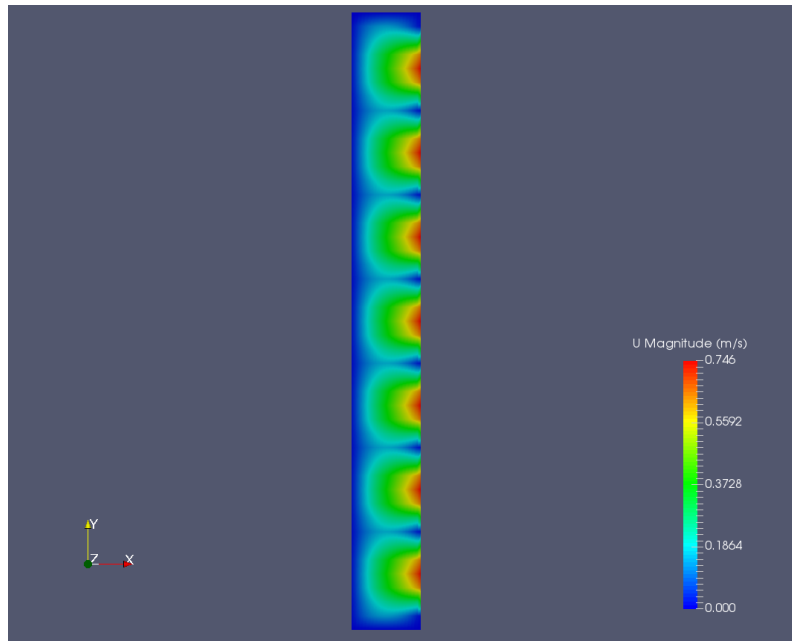


(a) Anode GDL velocity magnitude mid-height

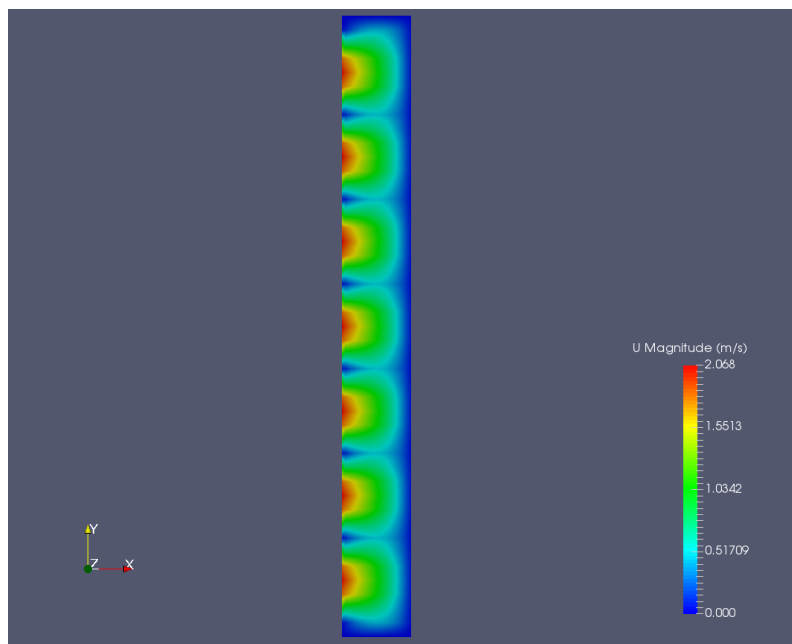


(b) Cathode GDL velocity magnitude mid-height

Figure 2.16: Reference case anode and cathode GDL velocity magnitude profile mid-height



(a) Anode GDL velocity magnitude mid-length



(b) Cathode GDL velocity magnitude mid-length

Figure 2.17: Reference case anode and cathode GDL velocity magnitude profile mid-length

Chapter 3

Variable Porosity & Manual Optimization

The toolbox selected to model the processes in the PEM fuel cell is insufficient for the goals of these thesis in one aspect. The porosity value used in the porous media is spatially constant in each medium. In order to be able to proceed with the optimization of the porosity distribution in the GDL, the toolbox has to be modified in order to account for variable porosity in the GDL. This is done by modifying the OpenFOAM code of the toolbox.

In order to investigate if changing the porosity value has an effect using the specified model, first of all a parametric study with spatially constant porosity values is done. After this is confirmed, the code is modified to account for variable porosity. Lastly, a first simplistic manual optimization of porosity is done to maximize voltage at low and high load using a simple porosity distribution.

3.1 Parametric Study of Constant Porosity

Before modifying the code to account for variable porosity in the GDL, it is of significant importance to investigate how the performance behaves under different values of the spatially constant porosity in the GDL. Thus, a parametric study of the constant porosity in the cathode GDL was carried out. All properties and parameter values, except for the cathode GDL porosity, are the same as in the reference case described in chapter 2.

It is important to note that this parametric study of porosity as well as any sub-

sequent work on variable porosity was done only for the cathode GDL and not the anode GDL as well. This is due to the fact that the phenomena that occur in the cathode and are handled by porosity attract more design attention. Apart from distributing the reactants in the CL and transporting electric charge which are done in both anode and cathode GDLs, the cathode GDL also transports the liquid water and serves to avoid flooding. For this reason, the parametric study and all subsequent work deals with the porosity in the cathode GDL while the porosity in the anode GDL is always constant.

Figure 3.1 displays the I-V curve for the various cathode GDL spatially constant porosity values ranging from 0.1 to 0.9. The current density or load ranges from 0 to $1.6 \frac{A}{cm^2}$. It is clear that the cathode GDL porosity value affects the performance of the PEM fuel cell. For very low porosity values, 0.1 to 0.3, the performance drops significantly. However, for very high porosity values as well, such as 0.9, the performance is affected negatively. The optimum region is for porosity values between 0.5 and 0.6. Note that in the reference case the porosity value is 0.5.

Figures 3.2, 3.3 and 3.4 show the overpotentials' curves for the various porosity values. These overpotentials provide an explanation for the effect that the porosity value has on the I-V curve. From figure 3.2 it can be observed that the activation overpotential is not really affected as the porosity does not affect significantly the reaction kinetics. The ohmic overpotential shown in figure 3.3 increases as the porosity value increases. This was expected since when porosity increases, conductivity decreases and resistance increases, leading to an increase in the ohmic overpotential. On the other hand, the concentration overpotential displayed in figure 3.4 decreases as the porosity value increases. This was also expected due to that higher porosity, meaning more empty space, allows easier transportation of the reactants to the CL which decreases the concentration overpotential.

So, on one hand it is clear that the porosity value in the model used affects the I-V curve. On the other hand, the porosity value should balance the trade off between easier transportation of reactants and liquid water and favorable conductivity of the GDL. This can also be seen in figures 3.5 and 3.6 which display, for loads of $0.6 \frac{A}{cm^2}$ and $1.2 \frac{A}{cm^2}$, the voltage output of the cell with regards to the porosity value of the cathode GDL. The optimal porosity value for the $0.6 \frac{A}{cm^2}$ case is 0.3 while for the $1.2 \frac{A}{cm^2}$ case is 0.5. This means that in the low load case, where liquid water formation is not particularly prevalent, lower porosity for higher conductivity is favored while in the high load case, conductivity is sacrificed for better flow of reactants and liquid water.

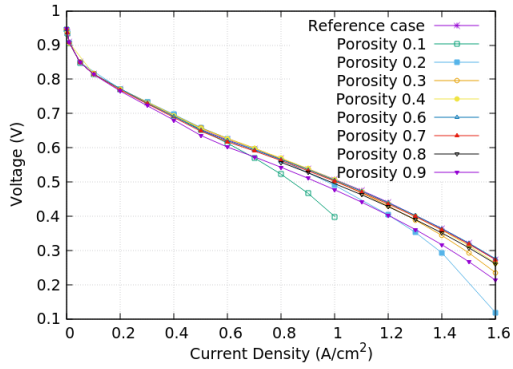


Figure 3.1: *I-V curve for the various cathode GDL porosity values ranging from 0.1 to 0.9*

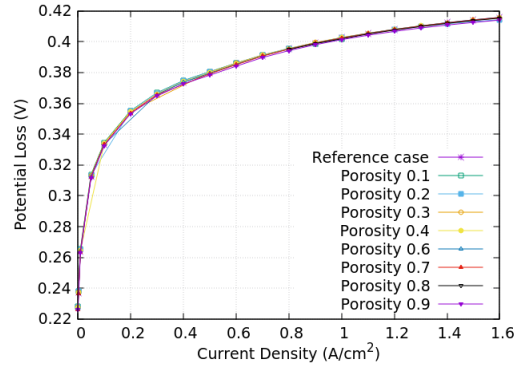


Figure 3.2: *Activation overpotentials for the various cathode GDL porosity values ranging from 0.1 to 0.9*

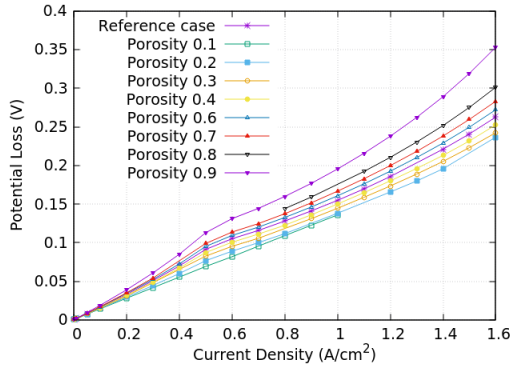


Figure 3.3: *Ohmic overpotentials for the various cathode GDL porosity values ranging from 0.1 to 0.9*

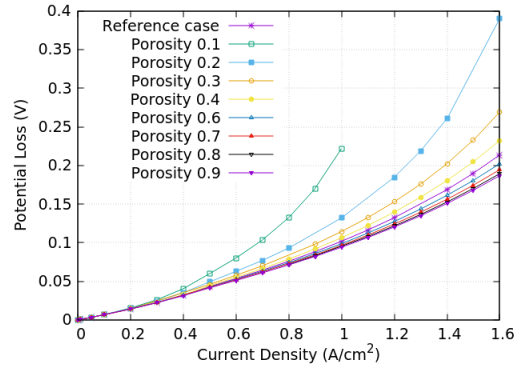


Figure 3.4: *Concentration overpotentials for the various cathode GDL porosity values ranging from 0.1 to 0.9*

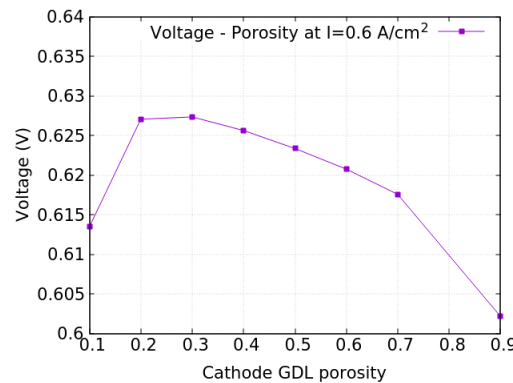


Figure 3.5: *Voltage vs Cathode GDL porosity value for load $I = 0.6 \frac{A}{cm^2}$*

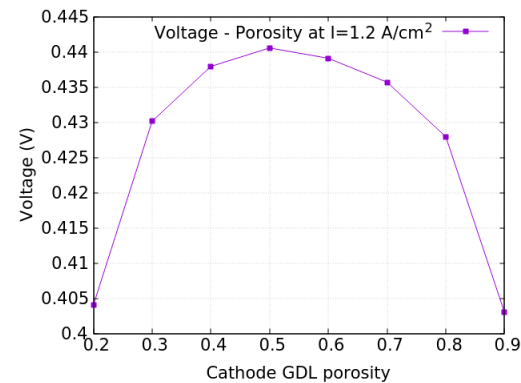


Figure 3.6: *Voltage vs Cathode GDL porosity value for load $I = 1.2 \frac{A}{cm^2}$*

3.2 Model Modifications for Variable Porosity

After confirming that in the model used the porosity value in the cathode GDL affects the performance, the toolbox is modified to account for variable porosity in the cathode GDL. To achieve this, the OpenFOAM code of the toolbox was modified. From an OpenFOAM coding perspective, changing the porosity from a spatially constant parameter to a spatially variable one did not pose considerable difficulties. It is, however, important to consider what should change in the equations of the model by accounting for variable porosity.

Most of the model parameters that porosity affects do not change whether porosity is a spatially constant or variable parameter. The parameters that are immediately affected by porosity are the mass source term S_l in equation (2.2), the effective diffusivity D_g^{eff} in equation (2.6), the effective electrical conductivity σ_e^{eff} in equation (2.21) and the capillary pressure p_c in equation (2.28). S_l , D_g^{eff} and p_c are already spatially variable as they include the spatially variable liquid water saturation in their formulas. However, σ_e^{eff} is not already spatially variable.

There are certain repercussions with changing σ_e^{eff} from a spatially constant parameter to a spatially variable one. In equation (2.20), the term

$$T_1 = \frac{\delta_{CGDL}}{\sigma_{eCGDL}^{eff}}$$

is produced by the more general term

$$T_2 = \int_0^{\delta_{CGDL}} \frac{dx}{\sigma_{eCGDL}^{eff}} = \int_0^{\delta_{CGDL}} \frac{dx}{\sigma_{eCGDL} (1 - \varepsilon_{CGDL})}$$

It is true that if ε_{CGDL} is constant then $T_1 = T_2$. However, that's not the case with spatially variable porosity. In that case, the term T_2 has to be computed as an integral. To avoid that, ε_{CGDL} is replaced with the averaged porosity in the cathode GDL, $\bar{\varepsilon}_{CGDL}$, to calculate T_2 . Thus

$$T_2 = \int_0^{\delta_{CGDL}} \frac{dx}{\sigma_{eCGDL}^{eff}} = \int_0^{\delta_{CGDL}} \frac{dx}{\sigma_{eCGDL} (1 - \bar{\varepsilon}_{CGDL})} = \frac{\delta_{CGDL}}{\sigma_{eCGDL} (1 - \bar{\varepsilon}_{CGDL})}$$

It is also important to note how the porosity is distributed and how it is inputted in the toolbox. For the subsequent work of this chapter, the porosity distribution selected to be used is linear from the BPP side to the CL side or, in other words, along the x direction. This linear profile along the x direction is selected for sev-

eral reasons. First of all, the work to be done next in this chapter is the manual optimization so the distribution needs to be as simple as possible. Secondly, it is considered that porosity distributions more complex than linear would be too complex to manufacture. Lastly, the x direction is considered to be the direction in which a porosity distribution would have the greatest effect and thus the linear distribution is imposed in the x direction for the manual optimization. As far as inputting the x direction linear profile of porosity in the cathode GDL goes, the porosity value at the cathode GDL cells closest to the BPP side and the porosity value at the cells closest to the CL side are imposed. Subsequently, the gradient is computed and the distribution is created by imposing the appropriate porosity value for every other cell in the cathode GDL.

3.3 "Manual" Optimization

As discussed earlier, before proceeding with the full optimization, a first simple "manual" optimization is carried out. This is done with a linear distribution of porosity in the cathode GDL along the x direction. The quantity to maximize is the voltage output at two different current densities of low and high load, $0.6 \frac{A}{cm^2}$ and $1.2 \frac{A}{cm^2}$.

The parameters that are being controlled for the optimization are the porosity value in the cathode GDL cells closest to the BPP and the porosity value in the cathode GDL cells closest to the CL. Seven values for these parameters are selected 0.05, 0.1, 0.3, 0.5, 0.7, 0.9 and 0.95 and thus 7×7 cases are run for each current density. The values selected cover most of the theoretically possible porosity value range which is 0 to 1. The extreme values are avoided as they would be practically not functional. Figure 3.7 displays a schematic of the cathode GDL seen from the BPP side to the CL side, with a random linear porosity distribution imposed and the various values of the porosity on each side.

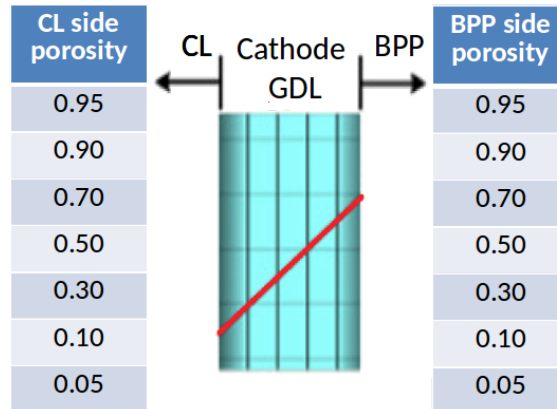


Figure 3.7: Schematic of the cathode GDL from BPP to CL with a random porosity distribution and the porosity values on each side.

Figure 3.8 displays the voltage map for both low and high load cases. Even though only the 49 cases mentioned were run, the voltage value was interpolated in the whole space. The porosity value closest to the CL side lies on the x axis while the porosity value closest to the BPP side lies on the y axis. The blue circle displays the reference case design while the green region is the optimal one in each case. The black regions denote cases/regions which did not converge mainly due to physical reasons as the porosity there is extremely low or high but, also, due to numerical instabilities.

In the low load case, the voltage range in the whole space is around 5% while in the high voltage case the voltage range is around 30% meaning that the porosity distribution affects the performance far more significantly in the high load case. This is due to the fact, as it can be observed, that in the high load case, low porosity values in the CL side cause an immediate drop in performance most probably due to the flooding effect present at high loads. Also, in the low load case, voltage is favored by lower porosity values in the CL side compared to the high load case while the optimal region's porosity values at the BPP side are almost the same in both cases. The reference case design, in both cases, lies in the optimal region. The voltage increase from the reference case to the optimized design is 0.4% in the low load case and 0.1% in the high load case.

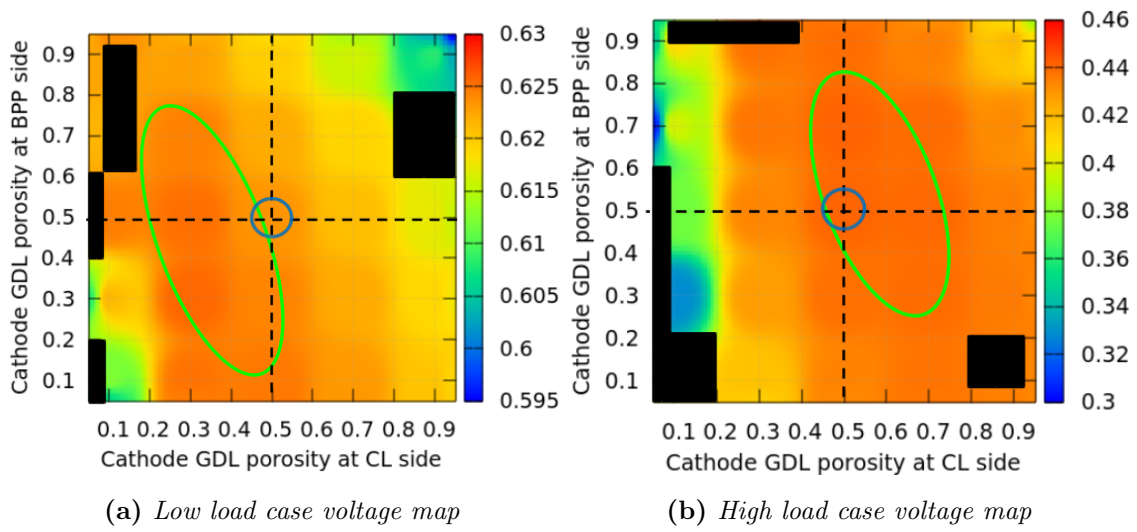


Figure 3.8: "Manual" optimization voltage maps at $0.6 \frac{A}{cm^2}$ and at $1.2 \frac{A}{cm^2}$. Blue circle displays the reference design and green denotes the optimal region.

Chapter 4

Optimization

After the "manual" optimization is completed, the full optimization can take place with more design variables and more complex cathode GDL porosity profiles. The full optimization is done using EASY, an EA-based optimization software [40]. The porosity distribution remains linear but is now imposed in all three directions of the cathode GDL.

4.1 Evolutionary Algorithms

Optimization methods [39] can be split into two main categories, gradient-based or deterministic methods and stochastic methods. Deterministic optimization methods use the general definition of the derivative of the objective function, which is required to be computed. On the other hand, stochastic methods, as the name suggests, are using randomized search to find the optimal solution. It is clear, therefore, that in order to use a deterministic method the computation of the derivatives of the objective function is necessary with respect to the design variables.

Evolutionary algorithms are the main representatives of the stochastic methods. They are based on principles derived from natural evolution, such as reproduction, mutation, recombination and selection. Basic characteristic of this method, in contrast with other stochastic methods, is that it uses a population of candidate solutions (population-based methods) instead of a single solution in every optimization iteration. The principles of natural evolution, mentioned above, can be translated into mathematical operators. The evolution of the population takes place after the repeated application of these operators with the goal of driving a population of candidate solutions towards better regions of the search space with respect to the selected objective function.

The main characteristics of an evolutionary algorithm can be summarized by the following

- They use populations of individuals (candidate solutions) which evolve simultaneously instead of single individuals.
- The evolution of the population is determined by the objective function values of its individuals.
- Populations must change dynamically by creating new individuals and eliminating other depending on their objective function value.
- During the evolution of the population, hereditary operations are employed. Features of the parent population should be found in the offspring population but new features must also appear.

Like every optimization method, evolutionary algorithms have both advantages and disadvantages in comparison with other methods.

One great disadvantage of an evolutionary algorithm, in its standard form, is that it requires a, relatively, large number of evaluations to identify the optimal solution. Therefore, the evaluation software, which is the expensive part of the optimization procedure, must be used a lot of times. Another disadvantage is that the more the design variables, the more the evaluations needed to actually find the optimal solution. Therefore, the computational cost greatly increases with the increase of the design variables. Nevertheless, there are methods that can reduce the total number of evaluations thus decreasing the total cost/time of an optimization procedure. Such a method is a metamodel assisted evolutionary algorithm. Metamodels replicate costly calls to the CFD evaluation software, by approximating the objective function at negligible cost, after training them on data collected from candidate solutions already evaluated, on the CFD tool, during the evolution.

On the other hand, evolutionary algorithms in contrast with deterministic methods will always find the global optimum of the problem, provided that an infinite number of evaluations can be performed. Another advantage is that, as already mentioned, an evolutionary algorithm can be used directly in a new problem without changing anything on the optimization software to fit the problem requirements. The only requirement for an EA is an output from the evaluation software with the value(s) of the objective function(s) for the individual to be evaluated.

Weighting the advantages and disadvantages of each optimization method it was decided that an EA better fits the requirements of the problem.

4.1.1 EA-Based Optimization

The EA-based optimization can be summarized in the following steps

1. Basic parameters, such as the size of the parent and offspring population, are selected, depending on the problem. The symbols $S^{g,\mu}$ and $S^{g,\lambda}$ correspond to the parent and offspring population, respectively. Letter g refers to the generation count. The procedure begins with a random selection of the individuals of $S^{0,\lambda}$.
2. The λ individuals of $S^{g,\lambda}$ are evaluated through the use of an evaluation software. After the flow fields are computed, a post-processor is used to compute the objective function of each individual.
3. The members of the elite population denoted by $S^{g,e}$ are renewed by the members of $S^{g,\lambda}$ that have a better objective function value. This step can be expressed as

$$S^{g+1,e} = T_e (S^{g,\lambda} \cup S^{g,e}) \quad (4.1)$$

where T_e is the operator identifying elite members.

There is always a chance that, at this step, no individual of $S^{g,\lambda}$ is better than the ones of $S^{g,e}$ and, therefore, the population of the elites remains the same. This is an indication that the EA did not manage to find a better solution in the last generation.

4. The elitism operator, T_{e2} , is used to replace individuals of $S^{g,\lambda}$ by individuals of $S^{g,e}$. Usually the worst individuals of the offspring population are chosen. Depending on the value of this operator, the search engine can be more elitistic or less elitistic. Through this step, getting a new generation (iteration) with an optimal solution worse than the one of the previous one, is avoided. This step can be expressed as

$$S^{g,\lambda} = T_{e2} (S^{g,\lambda} \cup S^{g+1,e}) \quad (4.2)$$

5. The new parent population $S^{g+1,\mu}$ is created through the use of the operator T_μ . Usually this is done through the use of the current offspring and parent population

$$S^{g+1,\mu} = T_\mu (S^{g,\mu} \cup S^{g,\lambda}) \quad (4.3)$$

6. The next step is the generation of a new offspring population, $S^{g+1,\lambda}$. To accomplish this, individuals of $S^{g+1,\mu}$ and $S^{g+1,e}$ are randomly selected. For each combination of parents selected, some operators, such as the mutation operator (T_m) and crossover operator (T_r), are used to produce the final offspring

population of the new generation.

$$S^{g+1,\lambda} = T_m T_r (S^{g+1,\mu} \cup S^{g+1,e}) \quad (4.4)$$

7. Convergence criteria for a single objective optimization, such as the optimal value remaining the same for N generations, are checked and, if satisfied, the algorithm stops. If not, a new generation begins by repeating steps 2 to 6.

4.1.2 EASY

The optimization software EASY (Evolutionary Algorithm SYstem) [40] is used for the optimization. EASY is a general purpose optimization platform developed by the PCopt/NTUA. It can be used for single-objective (SOO) and multi-objective (MOO), constrained or unconstrained optimization problems. EASY offers a variety of options, such as hybrid optimization (using both stochastic and gradient-based optimization techniques), metamodel assisted evolutionary algorithms etc.

For carrying out EA-based optimization in EASY, the sole necessities are the evaluation software, a pre-processor for providing each candidate solution's design variables' values to the evaluation software and a post-processor for providing the value(s) of the objective function(s) and the values of any constraints to EASY. For every candidate solution, EASY provides a file named task.dat with the number and values of the design variables. This file is pre-processed and inputted in the evaluation software. The evaluation software is run and the results, after being post-processed, are returned to EASY via the files task.res and task.cns containing the value(s) of the objective function(s) and the values of any constraints respectively.

4.2 3D Linear Porosity Distributions

In the "manual" design which was performed in the previous chapter, a linear porosity distribution along the x direction in the cathode GDL with two design variables was used. In the new optimization run, the linear character of the distribution is meant to be preserved, however it is to be imposed in all three directions and also having points where the gradient changes. The linear distribution is preserved because, as discussed earlier, more complex distributions could probably be non-manufacturable. In the x direction, there are two points of changing gradient, one half-way between the BPP side and the CL side and one three quarters of the way in from BPP to CL, where the MPL would be. This is a way to also take the MPL artificially into account. Thus, in the x direction, there are 4 design variables, the two porosity values at the CL side and BPP side and the two porosity values at

the two gradient changing points. In the z direction, there are again two points of changing gradient, one one third of the way in from inlet to outlet and one two thirds of the way in from inlet to outlet. Thus, in the z direction, there are also 4 design variables, the two porosity values at the inlet side and outlet side and the two porosity values at the two gradient changing points. In the y direction, it is selected to have a constant porosity value where the ribs of the BPP are and a different porosity value where the channels are. Thus, there are 2 design variables in the y direction, the two porosity values at the ribs and channels respectively, totaling 10 design variables. Figure 4.1 showcases these different linear profiles in the three directions.

Even though the distributions in each direction have been established, it has not yet been discussed how the porosity value for every cell in the internal field of the cathode GDL is calculated. There are several mathematical ways of achieving this. The mathematical formulation that was used goes as follows. Let ε_x , ε_y and ε_z be three independent quantities, each one describing the porosity distribution in each one direction as described above and shown in figure 4.1. Let \vec{b} be the design variable vector expressed as

$$\vec{b} = \{\vec{b}_x, \vec{b}_z, \vec{b}_y\} \quad (4.5)$$

$$\vec{b}_x = \{b_1, b_2, b_3, b_4\} \quad (4.6)$$

$$\vec{b}_z = \{b_5, b_6, b_7, b_8\} \quad (4.7)$$

$$\vec{b}_y = \{b_9, b_{10}\} \quad (4.8)$$

where \vec{b}_x , \vec{b}_z and \vec{b}_y are the design variables in the x , z and y directions respectively.

Then, if x_i , y_i and z_i are the coordinates of a cell, the three quantities ε_x , ε_y and ε_z are easy to compute and are expressed as

$$\varepsilon_x = \varepsilon_x(\vec{b}_x, x_i) \quad (4.9)$$

$$\varepsilon_y = \varepsilon_y(\vec{b}_y, y_i) \quad (4.10)$$

$$\varepsilon_z = \varepsilon_z(\vec{b}_z, z_i) \quad (4.11)$$

Lastly, the porosity ε of any cell is calculated as

$$\varepsilon(x_i, y_i, z_i, \vec{b}) = \varepsilon_x(\vec{b}_x, x_i) \cdot \varepsilon_y(\vec{b}_y, y_i) \cdot \varepsilon_z(\vec{b}_z, z_i) \quad (4.12)$$

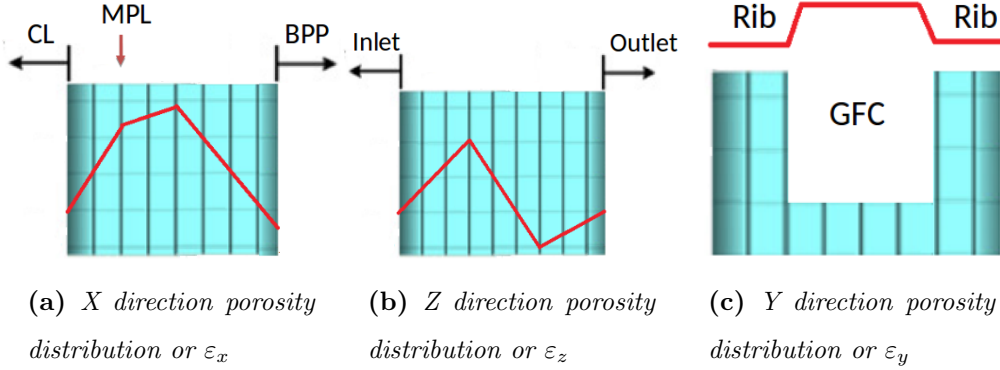


Figure 4.1: Complex linear porosity distributions along the three directions. Red line represents porosity.

There is a main advantage of this mathematical formulation compared to other formulations proposed but not used. This is that the porosity value of every internal cell is guaranteed to be between 0 and 1 as the product of ε_x , ε_y and ε_z . These quantities are by definition between 0 and 1 as long as every design variable b_i ranges between 0 and 1. The fact that every porosity value in the internal field of the cathode GDL is forced to be in this range means that no extra constraints have to be enforced in the optimization.

A counterexample of a formulation that would impose constraints and would not be favorable to use could be the following. Let S_j be a region where ε_x , ε_y and ε_z all have constant gradients. Let these gradients be a_{xj} , a_{yj} and a_{zj} respectively. If in all these regions S_j the porosity value of the included cells was given by

$$\varepsilon = a_{xj}x_i + a_{yj}y_i + a_{zj}z_i + b \quad (4.13)$$

where b is a constant, the resulting porosity in all points of changing gradient throughout the internal field would have to be constrained to range between 0 and 1. It can easily be proven that in such a case, the number of constraints would be proportional to N^3 where N is the number of design variables. Such a big number of constraints would make the optimization process really difficult.

4.3 Results

The optimization was carried out in EASY with the objective function being the voltage output of the cell which is to be maximized. Two cases were optimized, as in the "manual" optimization, at loads of $0.6 \frac{A}{cm^2}$ and $1.2 \frac{A}{cm^2}$. The design variables, which are 10, are as presented in the previous section and all have a minimum value

of 0 and a maximum value of 1. The design variables are binary encoded using 10 bits each.

As far as the search engine of EASY, is concerned the setup is the following. One deme is used with the population being 20 parents (μ) and 40 offspring (λ), each offspring being created by 3 parents. The mutation probability is 0.08. 1 elite is kept and forced as an offspring in each generation. Metamodels are used of the radial basis function (RBF) type. The minimum database entries required for the training of the metamodels is 150, 75 of which should be not failed while the patterns used for the training ranged from 20 to 50. Due to the small cost of the evaluation software, the evolution is allowed to expand for 1000 evaluations without imposing a limit on the idle generations.

The convergence history of both cases is shown in figure 4.2. Note that the x axis displays the number of successful evaluations and does not account for failed evaluations, thus why it does not reach 1000.

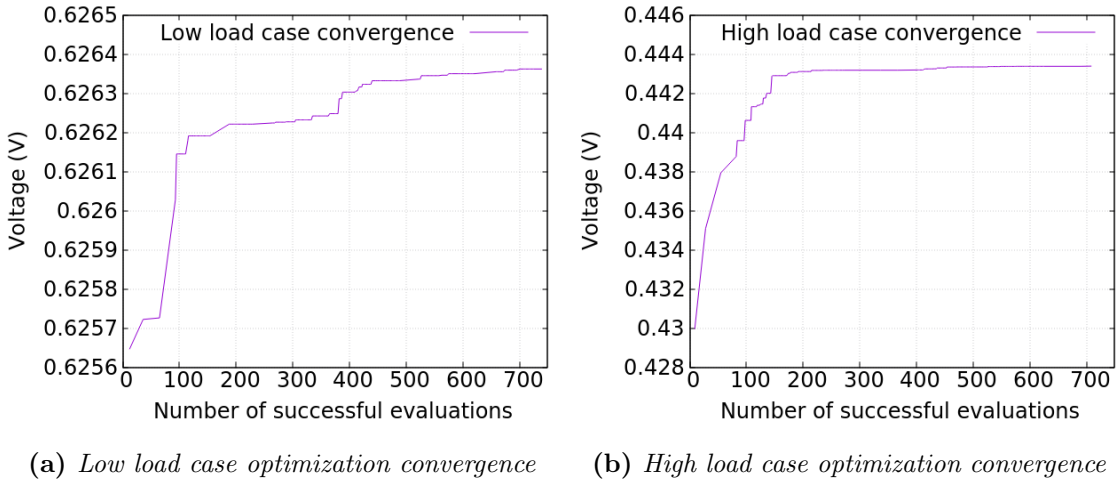
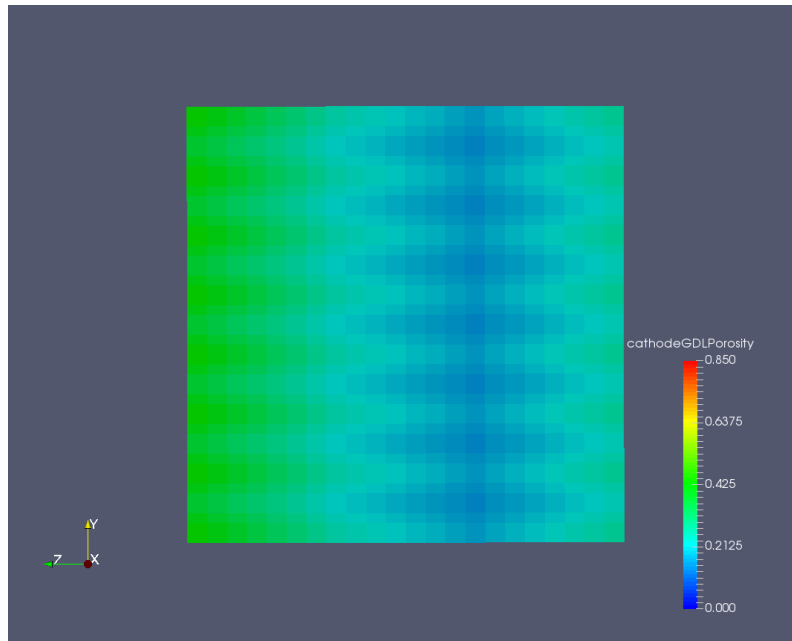


Figure 4.2: *Optimization convergence of both cases. X axis displays number of successful and not total evaluations.*

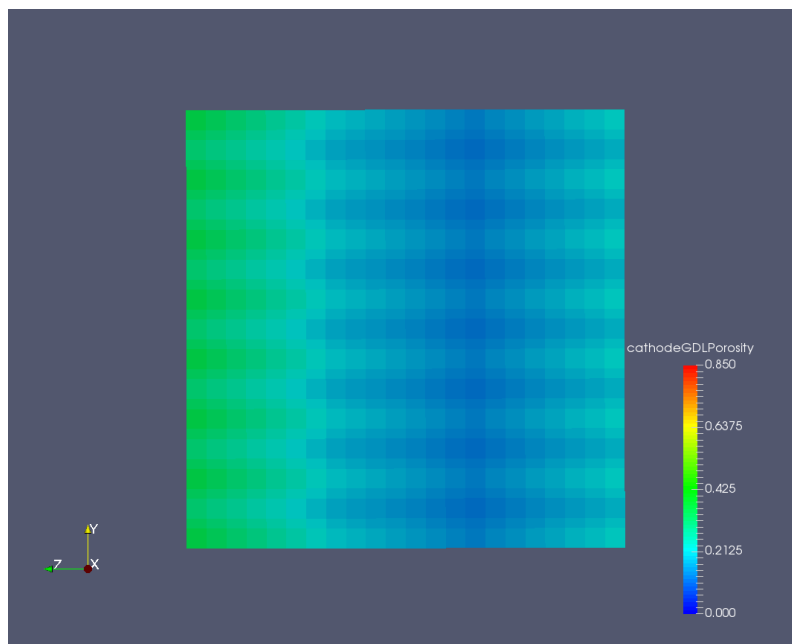
Figure 4.3 and 4.4 display the porosity profiles in the low and high load cases. As it is not possible to visualize simultaneously the porosity profile in the whole 3D field, slices are taken along the x direction closest to the BPP and the CL and in the points of changing gradient.

Several conclusions can be drawn from these profiles. First of all, the average porosity values in the high load case are much higher compared to the low load case. While the max porosity in the low load case is around 0.4, the max porosity in the high load case is around 0.85. This can be attributed to the fact that in the high load case, water removal is much more important than conductivity, so the porosity has to be higher. Another fact that justifies this point is the distribution along the y

axis. In the low load case, where conductivity is of higher importance, the porosity in the rib area, which is the conductive part, is higher than in the channel area. The opposite is true in the high load case, where porosity is higher in the channel area for the water to be removed more easily. As for the distribution along the x direction, in the low load case porosity decreases from BPP to halfway, increase from halfway to three quarters in (or where the MPL start) and stays almost constant from there to CL. In the high load case, porosity constantly decreases from BPP to CL which is what was expected to be the optimal case at all loads. Another observation that was not expected is that along the z direction, in both cases, porosity is higher near the inlet and outlet and lower midway. This favors the flow to enter fully near the inlet and exit fully near the outlet, possibly leading to less evenly distributed reactants to the CL.

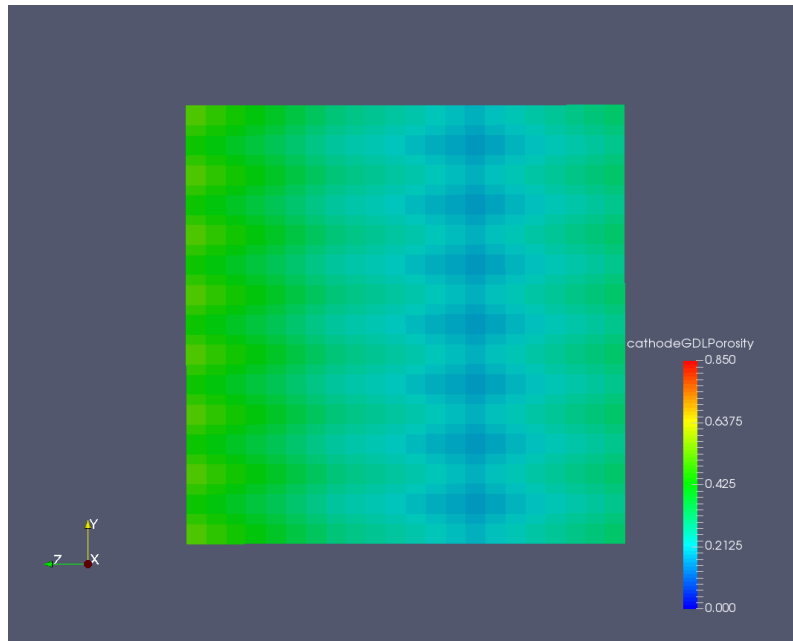


(a) *Low load case porosity distribution closest to BPP*

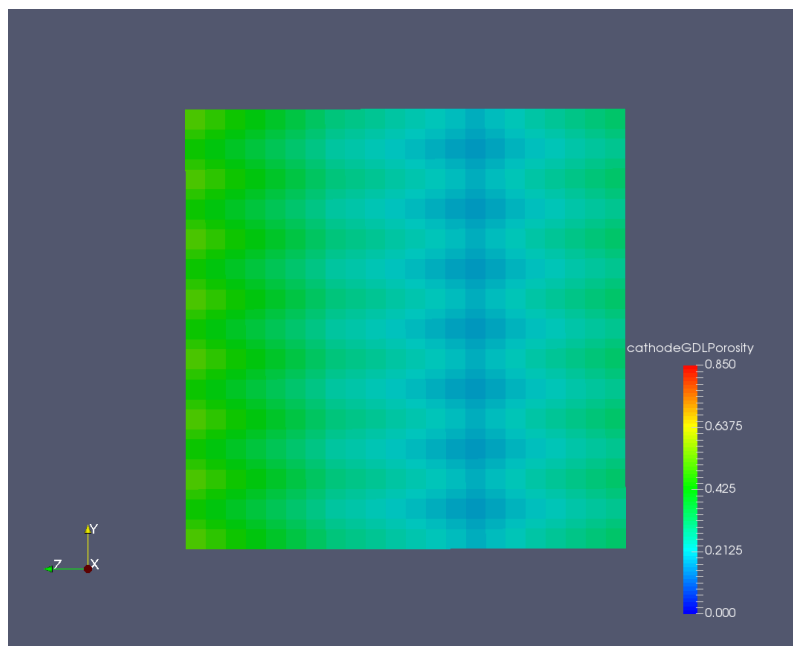


(b) *Low load case porosity distribution halfway*

Figure 4.3: *Low load case porosity distribution in slices along the x direction. Closest to BPP and CL and in points where the gradient changes. Continued in next page...*

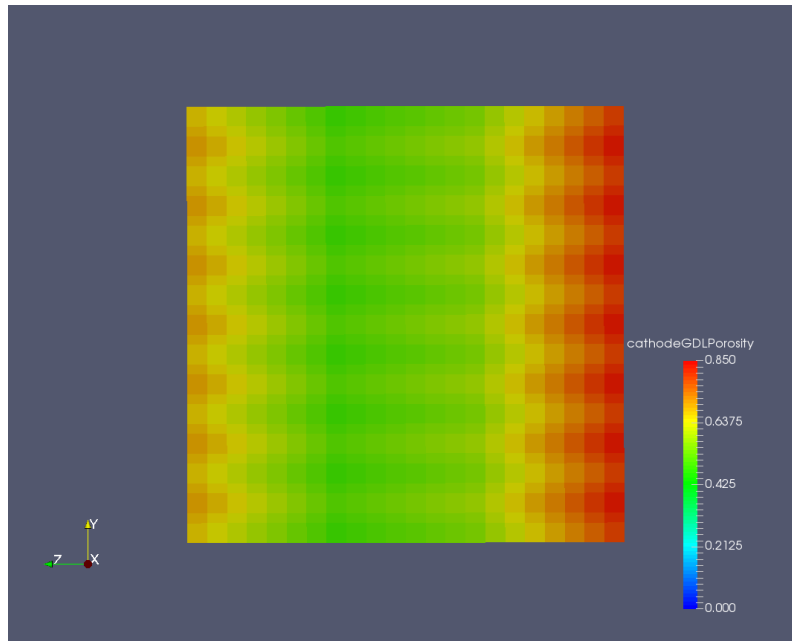


(c) *Low load case porosity distribution where the MPL begins*

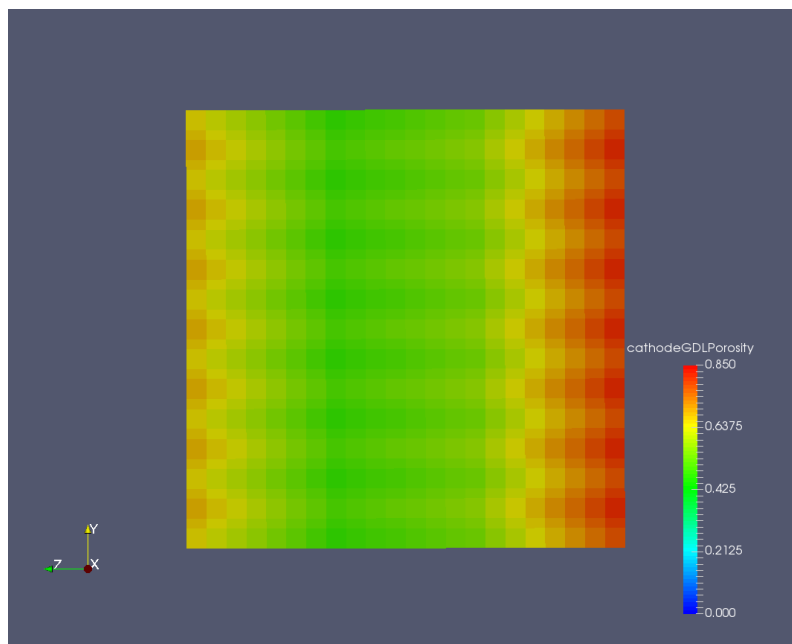


(d) *Low load case porosity distribution closest to CL*

Figure 4.3: *Low load case porosity distribution in slices along the x direction. Closest to BPP and CL and in points where the gradient changes.*

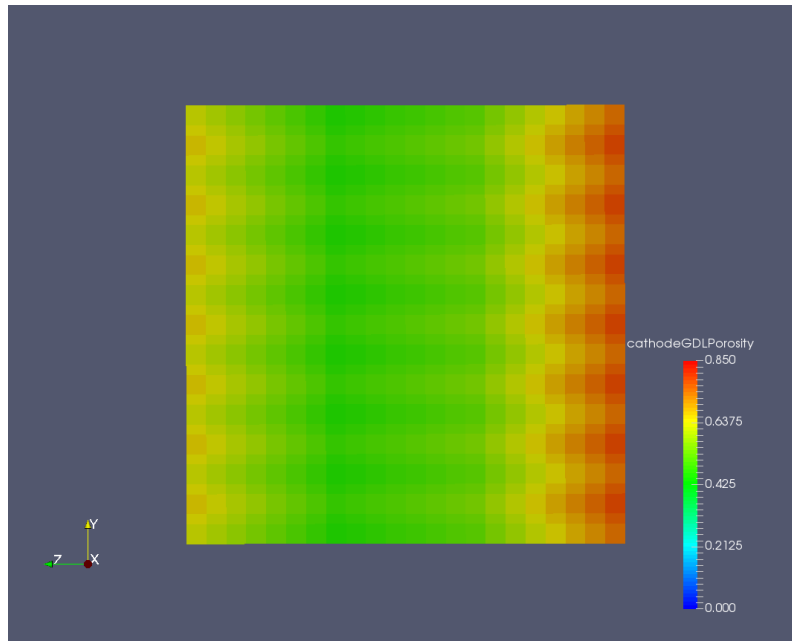


(a) *High load case porosity distribution closest to BPP*

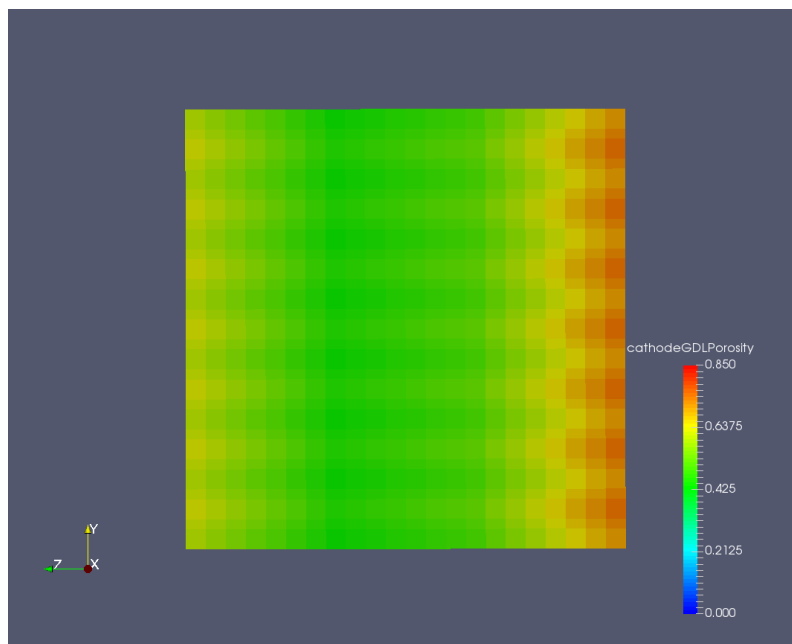


(b) *High load case porosity distribution halfway*

Figure 4.4: *High load case porosity distribution in slices along the x direction. Closest to BPP and CL and in points where the gradient changes. Continued in next page...*



(c) High load case porosity distribution where the MPL begins



(d) High load case porosity distribution closest to CL

Figure 4.4: High load case porosity distribution in slices along the x direction. Closest to BPP and CL and in points where the gradient changes.

Lastly, figure 4.5 displays quantitatively the comparison, for both cases, between the voltage output of the reference case, the "manual" optimization's design and the optimal design. First of all, it can be observed that the total gain in voltage

from the reference case to the optimal design is below 1%, being 0.5% in the low load case and 0.7% in the high load case. More interestingly, there is a big improvement from the "manual" design to the optimal one in the high load case and a far smaller one in the low load case. This implies that in the low load case, the porosity along the x direction, from BPP to CL is significantly more important than in the other two directions. The opposite is true in the high load case where the y and z directions are more important for porosity than the x direction. Again, this could potentially have to do with the liquid water management importance in the high load case, because of the complex nature of the phenomenon.

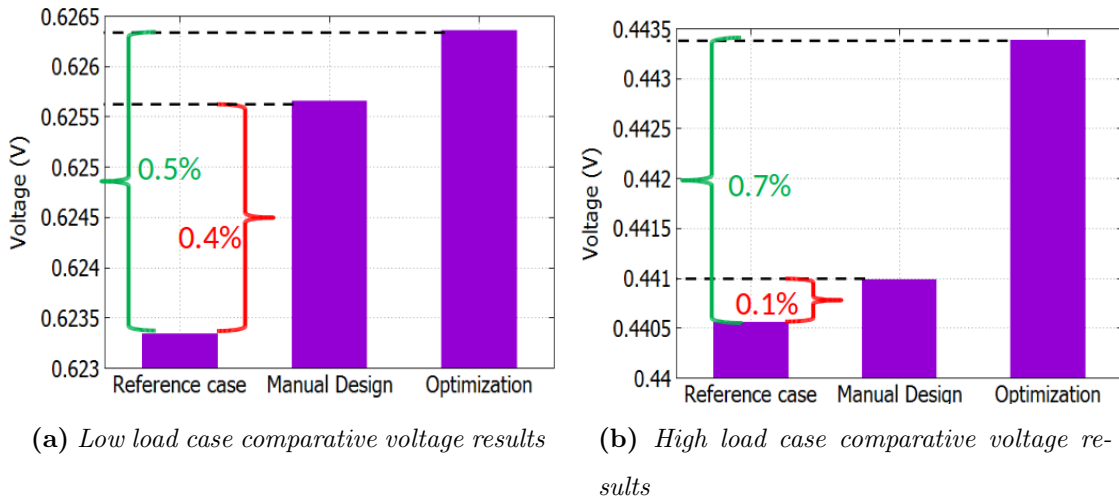


Figure 4.5: Comparison of voltage output for both low and high load cases between the reference case, the "manual" optimization's design and the optimal design.

Chapter 5

Overview and Conclusions

5.1 Overview

In this diploma thesis, the GDL component of a PEM fuel cell is studied, modeled and its porosity distribution is optimized.

A literature review was performed on the various and innovative approaches to modeling the GDL and especially the two-phase flow that takes place as it has a significant effect on the performance of the PEM fuel cell. Also, previous studies on optimizing the porosity of the GDL were reviewed.

An appropriate model of the whole PEM fuel cell and the corresponding OpenFOAM software toolbox was selected from literature and validated. For a reference case of certain operating conditions, the flow in the GDL as well as other results of interest throughout the whole fuel cell were produced and discussed.

The software was, then, adjusted to account for a spatially variable porosity distribution in the internal field of the cathode GDL. The cathode GDL was selected to be studied without including the anode GDL, as the cathode is of higher importance to the performance. A "manual" optimization was carried out for a low and high load case with a simple linear porosity distribution along the width (x) direction of the cathode GDL. This "manual" optimization showed that the reference case of constant porosity was already in the optimal region.

Lastly, the software was coupled with the EA-based optimization software EASY and a more complete optimization took place. Linear porosity distribution was preserved for manufacturability reasons, however porosity was distributed in all three directions. The appropriate mathematical formulation was presented, the low and high load cases were optimized and the results were discussed.

5.2 Conclusions

Based on the studies that were performed in the diploma thesis, the following conclusions are drawn :

1. The porosity value or distribution of the cathode GDL should balance a trade off between conductivity and ease of flow of both the reactants and the liquid water. The appropriate balance point varies depending on the operating load of the PEM fuel cell. Low load conditions favor lower porosity values than high load conditions. For high load conditions, low porosity values lead to non functionality of the fuel cell, as significant flooding of the cathode is caused.
2. The flow enters the GDL very close to the inlet of the GFCs and exits very close to the outlet of the GFCs. This behavior is maintained in the optimized case as well. In the optimized case the porosity is kept low near the GFC's inlet and outlet and higher in the middle. This was not expected as it was believed that the porosity in the middle between GFC inlet and outlet would be higher in order to lead to more distributed entry of the flow and distribution of the reactants to the CL.
3. In high load conditions, the optimized porosity distribution strictly decreases from the BPP side to the CL side as it was expected. This is also the reason why currently the MPL is used. However, in low load conditions, the porosity distribution decreases from the BPP side up to the middle between BPP and CL and, then, increases till the CL side. The BPP side and CL side porosity values are almost the same in this case.
4. In low load conditions, applying a porosity distribution in the width (x) direction is more significant than applying a porosity distribution in the other two directions. However, in high load conditions, the length (z) and height (y) directions are more significant for porosity than the width direction as the performance gain is higher when applying a porosity distribution in these two directions as well.

Bibliography

- [1] Millington B, Du S, Pollet BG. The Effect of Materials on Proton Exchange Membrane Fuel Cell Electrode Performance. *Journal of Power Sources* 2011; **196**(21): 9013–9017. doi:10.1016/j.jpowsour.2010.12.043
- [2] Smithsonian National Museum of American History. Collecting the History of Phosphoric Acid Fuel Cells. <https://americanhistory.si.edu/fuelcells/phos/pafcmain.htm>
- [3] Haile SM, Boysen DA, Chisholm, CRI, Merle RB. Solid acids as fuel cell electrolytes. *Nature* 2001; **410**(6831): 910–913. doi:10.1038/35073536
- [4] Stambouli AB. Solid oxide fuel cells (SOFCs): a review of an environmentally clean and efficient source of energy. *Renewable and Sustainable Energy Reviews* 2002; **6**(5): 433–455. doi:10.1016/S1364-0321(02)00014-X
- [5] Reifsnider K, Huang X, Ju G, Solasi R. Multi-scale modeling approaches for functional nano-composite materials. *Journal of Materials Science* 2006; **41**(20): 6751-6759. doi:10.1007/s10853-006-0214-5
- [6] Kleemann J, Finsterwalder F, Tillmetz W. Characterisation of mechanical behaviour and coupled electrical properties of polymer electrolyte membrane fuel cell gas diffusion layers. *Journal of Power Sources* 2009; **190**(1): 92-102. doi:10.1016/j.jpowsour.2008.09.026.
- [7] Ramasamy RP, Kumbur EC, Mennh MM, Liu W, Moore D, Murthy M. Investigation of macro and micro-porous layer interaction in polymer electrolyte fuel cells. *International Journal of Hydrogen Energy* 2008; **33**(13): 3351-3367. doi:10.1016/j.ijhydene.2008.03.053.
- [8] Dicks AL. The role of carbon in fuel cells. *Journal of Power Sources* 2006; **156**(2): 128-141. doi:10.1016/j.jpowsour.2006.02.054.
- [9] Chu HS, Yeh C, Chen F. Effects of porosity change of gas diffuser on performance of proton exchange membrane fuel cell. *Journal of Power Sources* 2003; **123**(1): 1-9. doi:10.1016/S0378-7753(02)00605-5.
- [10] Uchida M, Aoyama Y, Eda N, Ohta A. Investigation of the Microstructure in the Catalyst Layer and Effects of Both Perfluorosulfonate Ionomer and PTFE-

- Loaded Carbon on the Catalyst Layer of Polymer Electrolyte Fuel Cells. *Journal of the Electrochemical Society* 1995; **142**(12): 4143-4149. doi:10.1149/1.2048477.
- [11] Brandon N, Brett D. Engineering porous materials for fuel cell applications. *Philosophical Transactions of the Royal Society of London A: Mathematical, Physical and Engineering Sciences* 2006; **364**(1838): 147-159. doi:10.1098/rsta.2005.1684.
- [12] Kone JP, Zhang X, Yan Y, Hu G, Ahmadi G. Three-dimensional multiphase flow computational fluid dynamics models for proton exchange membrane fuel cell: A theoretical development. *The Journal of Computational Multiphase Flows* 2007; **9**(1): 3-25. doi:10.1177/1757482XI17692341
- [13] Sunden B, Faghri M. Transport phenomena in fuel cells. *Southampton: WIT Press.* 2005
- [14] Wang Y, Chen KS, Cho SC. PEM fuel cells: thermal and water management fundamentals. *New York: Momentum Press.* 2013
- [15] Tryggvason G, Scardovelli R, Zaleski S. Direct numerical simulations of gas-liquid multiphase flows. *Cambridge: Cambridge University Press.* 2011
- [16] Sui PC, Djilali N. Analysis of coupled electron and mass transport in the gas diffusion layer of a PEM fuel cell. *Journal of Power Sources* 2006; **161**(1) : 294-300. doi:10.1016/j.jpowsour.2006.03.079
- [17] Vynnycky M. On the modelling of two-phase flow in the cathode gas diffusion layer of a polymer electrolyte fuel cell. *Applied Mathematics and Computation* 2007; **189**(2) : 1560-1575. doi:10.1016/j.amc.2006.12.040
- [18] Kone JP, Zhang X, Yan Y, Adegbite S. An Open-Source Toolbox for Multiphase Flow Simulation in a PEM Fuel Cell. *Computer and Information Science* 2018; **11**(3) : 10-34. doi:10.5539/cis.v11n3p10
- [19] Zhan Z, Xiao J, Li D, Pan M, Yuan R. Effects of porosity distribution variation on the liquid water flux through gas diffusion layers of PEM fuel cells. *Journal of power Sources* 2006; **160**(2) : 1041-1048. doi:10.1016/j.jpowsour.2006.02.060
- [20] Secanell M, Carnes B, Suleman A, Djilali N. Numerical optimization of proton exchange membrane fuel cell cathodes. *Electrochimica Acta* 2007; **52**(7) : 2668-2682. doi:10.1016/j.electacta.2006.09.049
- [21] Secanell M, Karan K, Suleman A, Djilali N. Multi-variable optimization of PEMFC cathodes using an agglomerate model. *Electrochimica Acta* 2007; **52**(22) : 6318-6337. doi:10.1016/j.electacta.2007.04.028
- [22] Secanell M, Songprakorp R, Suleman A, Djilali N. Multi-objective optimization of a polymer electrolyte fuel cell membrane electrode assembly. *Energy & Environmental Science* 2008; **1**(3) : 378-388. doi:10.1039/B804654A

- [23] Huang Y-X, Cheng C-H, Wang X-D, Jang J-Y. Effects of porosity gradient in gas diffusion layers on performance of proton exchange membrane fuel cells. *Energy* 2010; **35**(12) : 4786-4794. doi:10.1016/j.energy.2010.09.011
- [24] Wang J. Analysis of Deformation of Gas Diffusion Layers and the Impact of Performance of PEM Fuel Cells. Division of Heat Transfer : Department of Energy Sciences, Lund University. 2017
- [25] Zhou J, Putz A, Secanell M. A mixed wettability pore size distribution based mathematical model for analyzing two-phase flow in porous electrodes. *Journal of the Electrochemical Society* 2017; **164**(6) : 530-539. doi:10.1149/2.0381706jes
- [26] Zhou J, Shukla S, Putz A, Secanell M. Analysis of the role of the microporous layer in improving polymer electrolyte fuel cell performance. *Electrochimica Acta* 2018; **268** : 366-382. doi:10.1016/j.electacta.2018.02.100
- [27] Niu Z, Bao Z, Wu J, Wang Y, Jiao K. Two-phase flow in the mixed-wettability gas diffusion layer of proton exchange membrane fuel cells. *Applied Energy* 2018; **232** : 443-450. doi:10.1016/j.apenergy.2018.09.209
- [28] Chen S, Doolen GD. Lattice Boltzmann Method for Fluid Flows. *Annual Review of Fluid Mechanics* 1998; **30**(1): 329–364. doi:10.1146/annurev.fluid.30.1.329
- [29] Hao L, Cheng P. Lattice Boltzmann simulations of water transport in gas diffusion layer of a polymer electrolyte fuel cell. *Journal of Power Sources* 2010; **195**(12) : 3870-3881. doi:10.1016/j.jpowsour.2009.11.125
- [30] Jinuntuya F, Whiteley M, Chen R, Fly A. The effects of gas diffusion layers structure on water transportation using X-ray computed tomography based Lattice Boltzmann method. *Journal of Power Sources* 2018; **378** : 53-65. doi:10.1016/j.jpowsour.2017.12.016
- [31] Xing L, Liu X, Alaje T, Kumar R, Mamlouk M, Scott K. A two-phase flow and non-isothermal agglomerate model for a proton exchange membrane (PEM) fuel cell. *Energy* 2014; **73** : 631-645. doi:10.1016/j.energy.2014.06.065
- [32] Nam JH, Kaviany M. Effective diffusivity and water-saturation distribution in single- and two-layer PEMFC diffusion medium. *International Journal of Heat and Mass Transfer* 2003; **46**(24) : 4595-4611. doi:10.1016/s0017-9310(03)00305-3
- [33] Nguyen TV, White RE. A water and heat management model for proton-exchange-membrane fuel cells. *Journal of the Electrochemical Society* 1993; **140**(8) : 2178-2186. doi:10.1149/1.2220792
- [34] Barbir F. PEM fuel cells: theory and practice. *London: Elsevier Academic*. 2005
- [35] Wang Y, Chen KS, Cho SC. PEM fuel cells: thermal and water management fundamentals. *New York: Momentum Press* 2013

- [36] O'Hayre RP, Cha SW, Colella W, Prinz FB. Fuel Cell Fundamentals. *New Jersey: John Wiley & Sons* 2006
- [37] Springer TE, Zawodzinski TA, Gottesfeld S. Polymer electrolyte fuel-cell model. *Journal of the Electrochemical Society* 1991; **138**(8) : 2334-2342. doi:10.1149/1.2085971
- [38] Yuan W, Tang Y, Pan MQ, Li ZT, Tang B. Model prediction of effects of operating parameters on proton exchange membrane fuel cell performance. *Renewable Energy* 2010; **35**(3) : 656-666. doi:10.1016/j.renene.2009.08.017
- [39] Giannakoglou KC. Optimization Methods in Aerodynamics. Notes. *NTUA, Athens*. 2005
- [40] EASY webpage. <http://velos0.ltt.mech.ntua.gr/EASY>.



Εθνικό Μετσόβιο Πολυτεχνείο

Σχολή Μηχανολόγων Μηχανικών

Τομέας Ρευστών

Μονάδα Παράλληλης Υπολογιστικής Ρευστοδυναμικής
& Βελτιστοποίησης

Μοντελοποίηση & Βελτιστοποίηση Στρώματος
Διάχυσης Αερίου Κυψελών Καυσίμου και Πορώδους
στο OpenFOAM

Διπλωματική Εργασία

Πέτρος Π. Λαμπρινίδης

Επιβλέπων :

Κυριάκος Χ. Γιαννάκογλου, Καθηγητής ΕΜΠ

Βιομηχανικός Επιβλέπων :

Δρ. Κωνσταντίνος Γκαγκάς, Ειδικός Toyota Motor Europe

Αθήνα, Φεβρουάριος 2021

Εκτενής Περίληψη στα Ελληνικά

Εισαγωγή

Οι κυψέλες καυσίμου αποκτούν αυξανόμενο ερευνητικό ενδιαφέρον ως εναλλακτική πηγή καθαρής και βιώσιμης ενέργειας για να αντικαταστήσουν τα ορυκτά καύσιμα. Στην αυτοκινητοβιομηχανία, επικρατούν οι κυψέλες καυσίμου μεμβράνης ανταλλαγής πρωτονίων (Proton Exchange Membrane, PEM) λόγω της υψηλής πυκνότητας ισχύος και των χαμηλών θερμοκρασιών λειτουργίας. Ένα από τα συστατικά στοιχεία της κυψέλης καυσίμου που έχει εξαιρετική επιρροή στην απόδοση είναι το Στρώμα Διάχυσης Αερίου (Gas Diffusion Layer, GDL) λόγω των ποικίλων φαινομένων που λαμβάνουν

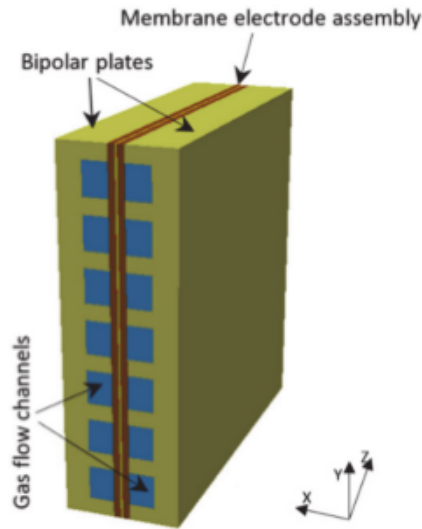
χώρα εκεί.

Σε αυτήν τη διπλωματική εργασία, το GDL μίας κυψέλης καυσίμου PEM μοντελοποιείται και βελτιστοποιείται ως προς το πορώδες του. Πρόσφατες έρευνες έχουν μελετήσει καινοτόμους τρόπους για τον έλεγχο της κατανομής πορώδους του GDL κατά την κατασκευή. Το πορώδες που χρησιμοποιείται σήμερα στο GDL είναι σταθερό. Είναι σημαντικό, επομένως, να μελετηθεί αριθμητικά εάν μια μη-σταθερή κατανομή πορώδους θα είχε ευνοϊκή επίδραση στην απόδοση της κυψέλης καυσίμου.

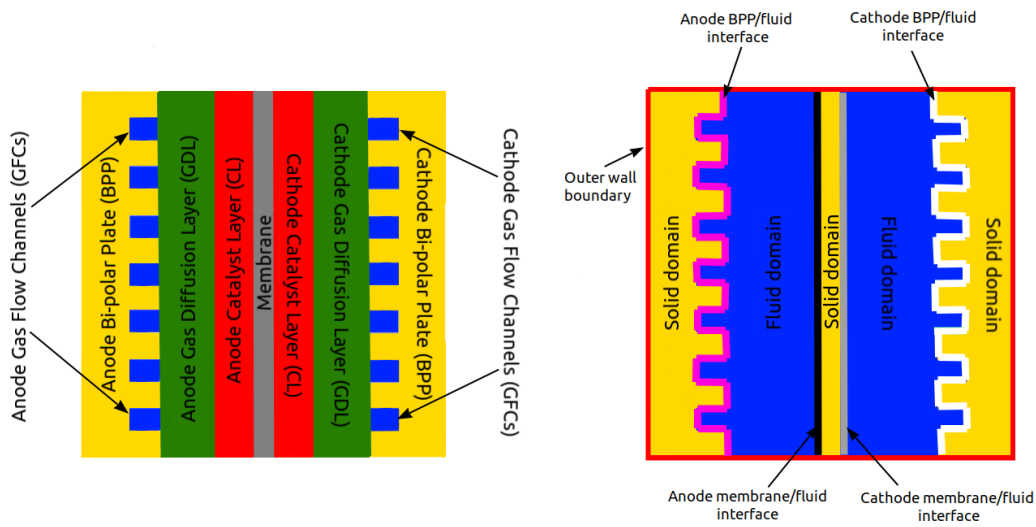
Μοντέλο & Εξισώσεις

Το μαθηματικό μοντέλο ανάλυσης μιας δεδομένης κυψέλης καυσίμου PEM επιλέγεται από τη βιβλιογραφία. Αποτελείται από τις εξισώσεις Navier-Stokes που έχουν τροποποιηθεί ώστε να ληφθούν υπόψη τα διάφορα ηλεκτρικά, θερμικά και χημικά φαινόμενα, μια επιπλέον εξίσωση που αντιστοιχεί στη διφασική ροή που λαμβάνει χώρα και μια επιπλέον εξίσωση για τη διατήρηση των χημικών στοιχείων. Το μοντέλο αναπτύσσεται και προσομοιώνεται σε περιβάλλον OpenFOAM.

Στο σχήμα 1 παρουσιάζεται η γεωμετρία της κυψέλης καυσίμου PEM που χρησιμοποιείται στο μοντέλο. Το υπολογιστικό χωρίο διαιρείται σε δύο χωρία, το υγρό και το στερεό χωρίο. Το υγρό χωρίο περιλαμβάνει για την άνοδο και την κάθοδο τα Κανάλια Ροής Αερίου (Gas Flow Channels, GFCs), το Στρώμα Διάχυσης Καυσίμου (GDL) και το Στρώμα Καταλύτη (Catalyst Layer, CL). Το στερεό χωρίο περιλαμβάνει τις διπολικές πλάκες (Bi-polar Plates, BPPs) για την άνοδο και την κάθοδο καθώς και τον ηλεκτρολύτη ή μεμβράνη (Membrane). Στο υγρό χωρίο λύνονται οι εξισώσεις Navier-Stokes, η εξίσωση διατήρησης των χημικών στοιχείων και η εξίσωση μεταφοράς του υγρού νερού. Στο στερεό χωρίο επιλύεται μόνο η εξίσωση διατήρησης ενέργειας λόγω της μεταφοράς θερμότητας. Οι ηλεκτροχημικές εξισώσεις και ο υπολογισμός της τάσης επιλύονται στη διεπιφάνεια της μεμβράνης και του υγρού χωρίου της καθόδου. Στο σχήμα 2 παρουσιάζονται διδιάστατα οι διάφορες συνιστώσες που αποτελούν την κυψέλη καυσίμου και τα δύο χωρία επίλυσης των εξισώσεων, υγρό και στερεό, καθώς και τα όρια αυτών.



Σχήμα 1: Γεωμετρία της κυψέλης καυσίμου PEM.



(i) Σχηματικό των διαφόρων συστατικών της κυψέλης καυσίμου.

(ii) Σχηματικό των χωρίων επίλυσης και των ορίων αυτών.

Σχήμα 2: Διδιάστατα σχηματικά των συστατικών της κυψέλης καυσίμου, των χωρίων επίλυσης και των ορίων αυτών.

Οι βασικές εξισώσεις του μοντέλου είναι

- Διατήρηση μάζας

$$\nabla \cdot (\rho_g \vec{U}_g) + S_l = 0 \quad (1)$$

- Διατήρηση ορμής

$$\nabla \cdot (\rho_g \vec{U}_g \vec{U}_g) = -\nabla p_g + \nabla \cdot (\mu_g \nabla \vec{U}_g) + S_M \quad (2)$$

- Διατήρηση χημικών στοιχείων

$$\nabla \cdot (\rho_g \vec{U}_g y_i) = \nabla \cdot (\rho_g D_{g,i}^{eff} \nabla y_i) \quad (3)$$

- Διατήρηση ενέργειας στο υγρό χωρίο

$$\nabla \cdot (\rho_{mix} c_{p_{mix}} \vec{U}_g T) = \nabla \cdot (k_{mix} \nabla T) + S_E^{PC} \quad (4a)$$

Διατήρηση ενέργειας στη μεμβράνη

$$\nabla \cdot (k_{solid} \nabla T) + S_E^{reac} = 0 \quad (4b)$$

Διατήρηση ενέργειας στις διπολικές πλάκες

$$\nabla \cdot (k_{solid} \nabla T) = 0 \quad (4c)$$

- Μεταφορά υγρού νερού

$$\nabla \cdot (\rho_l D_l \nabla s) - \nabla \cdot (\rho_g \vec{U}_g s) + S_l = 0 \quad (5)$$

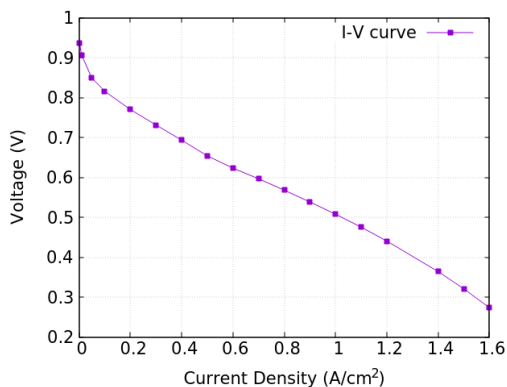
- Τάση κυψέλης καυσίμου

$$V_{cell} = E_{Nernst} - \eta_{act} - \eta_{ohm} - \eta_{con} \quad (6)$$

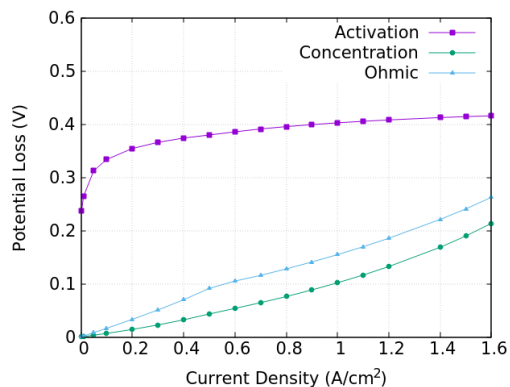
Οι όροι των εξισώσεων καθώς και η ανάλυση αυτών σε περαιτέρω εξισώσεις παρουσιάζονται εκτενώς στο κυρίως κείμενο.

Για την περίπτωση αναφοράς που επιλέγεται και αναλύεται στο κυρίως κείμενο, το σχήμα 3 παρουσιάζει την καμπύλη πόλωσης ή καμπύλη I-V που προκύπτει ενώ το σχήμα

4 παρουσιάζει τις καμπύλες των διαφόρων απωλειών τάσης. Το σχήμα 5 παρουσιάζει την ταχύτητα και τις γραμμές ροής στο GDL στο μέσο του κεντρικού καναλιού της καθόδου και δείχνει εμφανώς την τάση της ροής να κινείται εντός του GDL σχεδόν παράλληλα από την είσοδο προς την έξοδο.



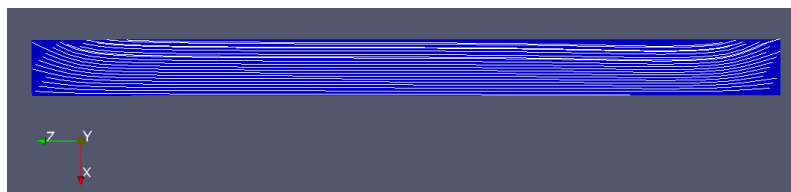
Σχήμα 3: Καμπύλη πόλωσης για τις παραμέτρους της περίπτωσης αναφοράς.



Σχήμα 4: Καμπύλες απωλειών τάσης για τις παραμέτρους της περίπτωσης αναφοράς.



(i) Ταχύτητα στο GDL της καθόδου.



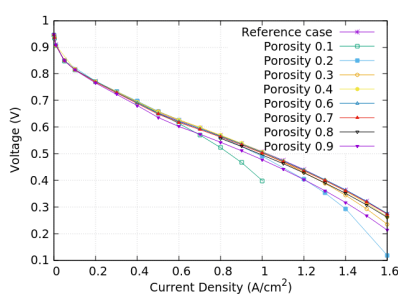
(ii) Γραμμές ροής στο GDL της καθόδου.

Σχήμα 5: Ταχύτητα και γραμμές ροής στο GDL στο μέσο του κεντρικού καναλιού της καθόδου για την περίπτωση αναφοράς.

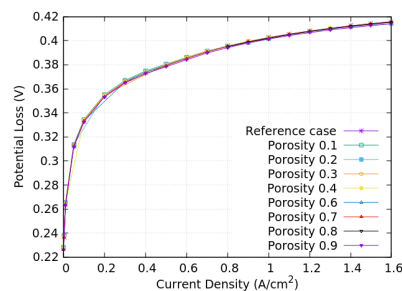
Μεταβλητό Πορώδες & Απλή Βελτιστοποίηση

Στο μοντέλο που επιλέχθηκε για τη μοντελοποίηση της κυψέλης καυσίμου PEM, το πορώδες του GDL είναι χωρικά σταθερό. Με σκοπό να γίνει η βελτιστοποίηση κατανομής του πορώδους, το μοντέλο πρέπει να τροποποιηθεί ώστε να λαμβάνει υπόψη χωρικά μεταβλητό πορώδες στο GDL. Η διαδικασία αυτή επιλέχθηκε να πραγματοποιηθεί για το GDL της καθόδου καθώς τα φαινόμενα που λαμβάνουν χώρα εκεί είναι πιο σημαντικά για την απόδοση της κυψέλης καυσίμου.

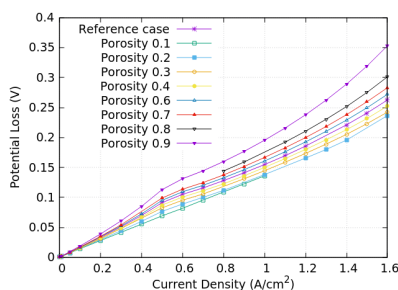
Αρχικά, για να μελετηθεί αν η τιμή του πορώδους έχει αντίκτυπο στην απόδοση της κυψέλης καυσίμου, παράγεται η καμπύλη πόλωσης με τις παραμέτρους της περίπτωσης αναφοράς αλλά για διάφορες τιμές του χωρικά σταθερού πορώδους του GDL της καθόδου. Η καμπύλη αυτή παρουσιάζεται στο σχήμα 6. Τα σχήματα 7, 8 και 9 παρουσιάζουν τις αντίστοιχες καμπύλες των διαφόρων απωλειών τάσης.



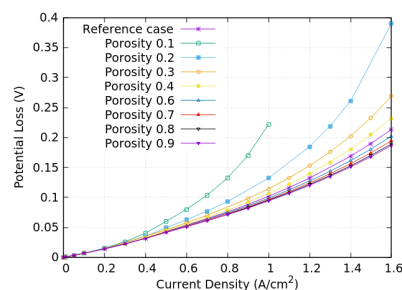
Σχήμα 6: Καμπύλη πόλωσης για διάφορες χωρικά σταθερές τιμές του πορώδους του GDL της καθόδου.



Σχήμα 7: Καμπύλη απώλειας ενεργοποίησης για διάφορες χωρικά σταθερές τιμές του πορώδους του GDL της καθόδου.



Σχήμα 8: Καμπύλη ωμικής απώλειας για διάφορες χωρικά σταθερές τιμές του πορώδους του GDL της καθόδου.

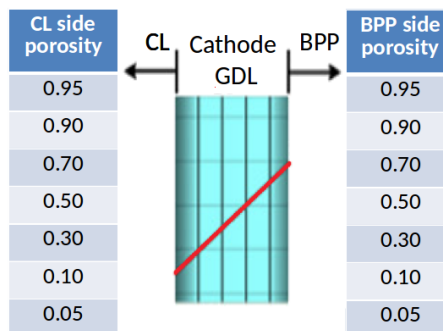


Σχήμα 9: Καμπύλη απώλειας συγκέντρωσης για διάφορες χωρικά σταθερές τιμές του πορώδους του GDL της καθόδου.

Στη συνέχεια το μοντέλο τροποποιείται από άποψη κώδικα για να λαμβάνει υπόψη χωρικά μεταβλητό πορώδες στο GDL της καθόδου. Οι εξισώσεις του μοντέλου παραμέ-

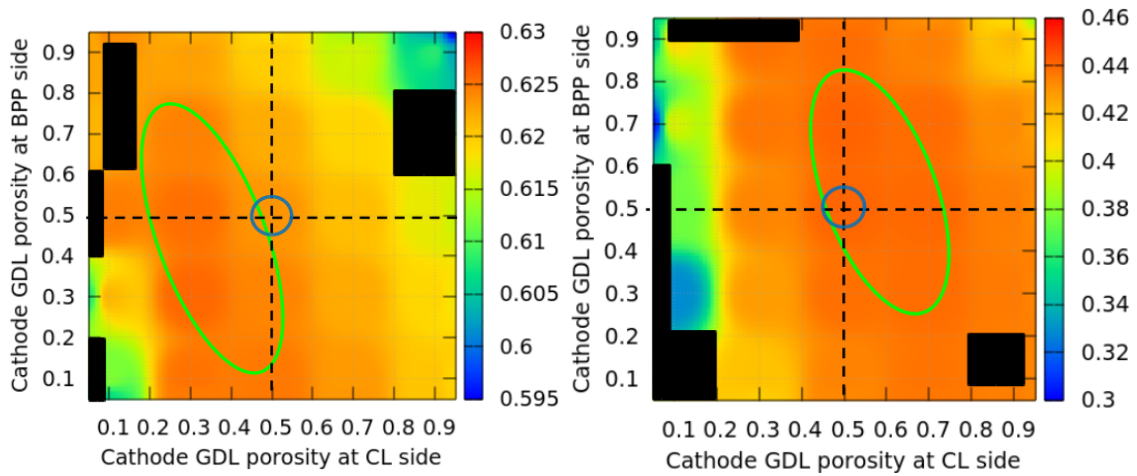
νουν, στο μεγαλύτερο τμήμα τους, απaráλλαχτες καθώς δεν επηρεάζονται από τη χωρική σταθερότητα ή μεταβλητότητα του πορώδους.

Τέλος, πραγματοποιείται απλή "χειροκίνητη" βελτιστοποίηση με μία γραμμική κατανομή του πορώδους στο GDL της καθόδου κατά τη διεύθυνση από τη διπολική πλάκα (BPP) προς το στρώμα καταλύτη (CL). Η ποσότητα για μεγιστοποίηση είναι η τάση της κύψελης καυσίμου σε δύο περιπτώσεις χαμηλού και υψηλού φορτίου. Επιβάλλονται 7 διαφορετικές τιμές του πορώδους στις δύο πλευρές όπως φαίνεται στο σχηματικό του σχήματος 10.



Σχήμα 10: Σχηματικό του GDL της καθόδου από τη BPP στο CL με τη γραμμική κατανομή πορώδους και τις διάφορες τιμές στις δύο πλευρές.

Στο σχήμα 11 παρουσιάζεται ο χάρτης της τάσης για τις δύο περιπτώσεις χαμηλού και υψηλού φορτίου. Οι μαύρες περιοχές είναι περιοχές όπου το μοντέλο δεν συνέκλινε είτε λόγω φυσικών είτε λόγω αριθμητικών αιτιών. Παρατηρείται πως στην περίπτωση χαμηλού φορτίου η βέλτιστη περιοχή έγκειται σε μικρότερες τιμές του πορώδους στην πλευρά του CL ενώ στην περίπτωση υψηλού φορτίου υψηλότερες τιμές στην πλευρά του CL είναι βέλτιστες. Όσον αφορά τη βέλτιστη τιμή του πορώδους στην πλευρά της BPP, είναι σχεδόν ίδια και στις δύο περιπτώσεις. Η περίπτωση αναφοράς έγκειται εντός των βέλτιστων περιοχών και στις δύο περιπτώσεις και η αύξηση της τάσης από την περίπτωση αναφοράς στο βέλτιστο σχεδιασμό είναι πολύ μικρή σε αμφότερα φορτία.



(i) Χάρτης τάσης σε χαμηλό φορτίο.

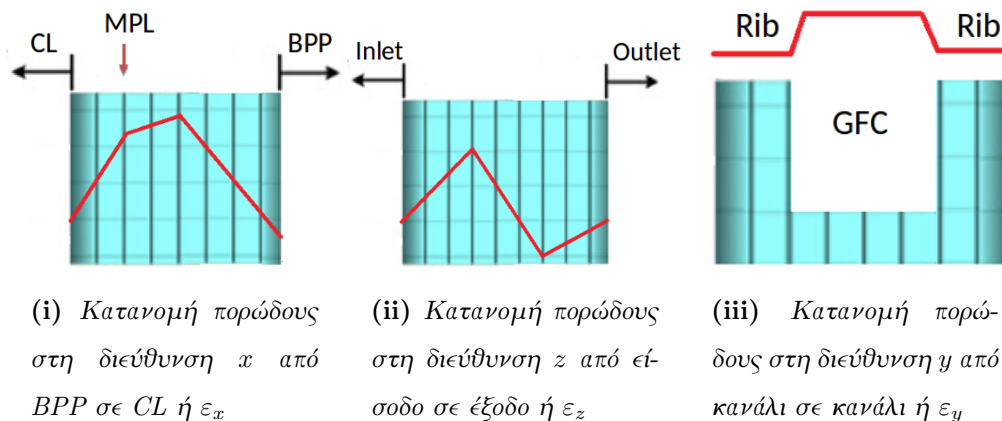
(ii) Χάρτης τάσης σε υψηλό φορτίο.

Σχήμα 11: Χάρτες τάσης απλής βελτιστοποίησης σε χαμηλό και υψηλό φορτίο. Ο μπλέ κύκλος παρουσιάζει την περίπτωση αναφοράς ενώ η βέλτιστη περιοχή παρουσιάζεται με πράσινο.

Βελτιστοποίηση

Τέλος, πραγματοποιείται η πλήρης βελτιστοποίηση με πιο περίπλοκες κατανομές πορώδους για μεγιστοποίηση της τάσης σε χαμηλό και υψηλό φορτίο χρησιμοποιώντας το λογισμικό EASY του EMPI το οποίο βασίζεται σε εξελικτικούς αλγορίθμους. Η κατανομή πορώδους παρόλο που παραμένει γραμμική, είναι πλέον τριδιάστατη και σε κάθε διάσταση έχει πλέον σημεία αλλαγής της κλίσης. Οι μεταβλητές σχεδιασμού είναι συνολικά 10, 4 στη διεύθυνση από BPP σε CL (2 τιμές στις πλευρές και 2 τιμές στα σημεία αλλαγής κλίσης), 4 στη διεύθυνση από είσοδο σε έξοδο (2 τιμές στις πλευρές και 2 τιμές στα σημεία αλλαγής κλίσης) και 2 στη διεύθυνση από κανάλι σε κανάλι (1 τιμή καθ' ύψος κάθε νεύρου της BPP και 1 τιμή καθ' ύψος κάθε καναλιού). Οι γραμμικές κατανομές σε κάθε διεύθυνση παρουσιάζονται στο σχήμα 12. Έστω ε_x , ε_y και ε_z οι γραμμικές αυτές κατανομές στις διευθύνσεις x , y και z αντίστοιχα. Τότε, το πορώδες σε κάθε εσωτερικό σημείο του χωρίου με συντεταγμένες x_i , y_i , z_i προκύπτει ως

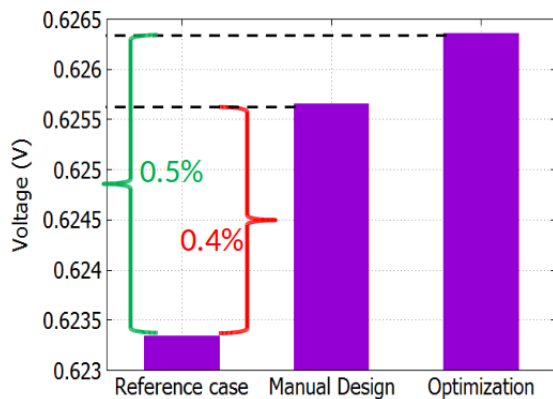
$$\varepsilon(x_i, y_i, z_i) = \varepsilon_x(x_i) \cdot \varepsilon_y(y_i) \cdot \varepsilon_z(z_i) \quad (7)$$



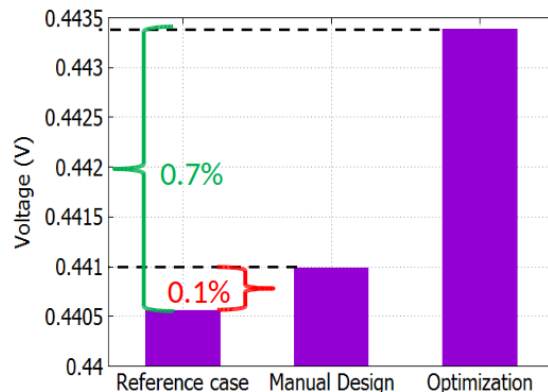
Σχήμα 12: Γραμμικές κατανομές πορώδους στις τρεις διευθύνσεις. Η κόκκινη γραμμή αντιπροσωπεύει το πορώδες.

Από τις βελτιστοποιημένες κατανομές που προκύπτουν παρατηρείται ότι, για υψηλό φορτίο, η μέση τιμή του πορώδους είναι πολύ υψηλότερη από ό,τι για χαμηλό φορτίο. Για χαμηλό φορτίο, κατά τη διεύθυνση y , η τιμή του πορώδους είναι υψηλότερη καθ' ύψος των νευρών σε σχέση με την τιμή καθ' ύψος των καναλιών ενώ το αντίθετο συμβαίνει για υψηλό φορτίο. Στη διεύθυνση x , για χαμηλό φορτίο το πορώδες μειώνεται από την πλευρά της BPP έως το μέσο της διεύθυνσης, αυξάνεται έως τα τρία τρίτα της διεύθυνσης όπου βρίσκεται το στρώμα μικροπορώδους (MPL) και από εκεί μένει σταθερό έως την πλευρά του CL. Στην ίδια διεύθυνση, για υψηλό φορτίο, το πορώδες μειώνεται αυστηρά από την πλευρά της BPP έως την πλευρά του CL. Στη διεύθυνση z , για αμφότερα φορτία, το πορώδες είναι υψηλότερο κοντά στην είσοδο και στην έξοδο και χαμηλότερο ενδιάμεσα.

Τέλος, στο σχήμα 13 παρουσιάζεται η σύγκριση της τάσης της κυψέλης καυσίμου, για αμφότερα φορτία, στην περίπτωση αναφοράς, στον απλό "χειροκίνητο" βελτιστοποιημένο σχεδιασμό και στον πλήρη βέλτιστο σχεδιασμό. Για αμφότερα φορτία, η αύξηση της τάσης από την περίπτωση αναφοράς στον βέλτιστο σχεδιασμό είναι μικρότερη του 1%. Η αύξηση της τάσης από τον "χειροκίνητο" σχεδιασμό στον βέλτιστο σχεδιασμό είναι πολύ μεγαλύτερη για υψηλό φορτίο σε σχέση με το χαμηλό φορτίο. Αυτό υπονοεί πως η τιμή του πορώδους κατά τη διεύθυνση x είναι πιο σημαντική στο σχεδιασμό στο χαμηλό φορτίο, ενώ η τιμή στις άλλες δύο διευθύνσεις είναι πιο σημαντική στο σχεδιασμό στο υψηλό φορτίο.



(i) Συγκριτικά αποτελέσματα τάσης στο χαμηλό φορτίο.



(ii) Συγκριτικά αποτελέσματα τάσης στο υψηλό φορτίο.

Σχήμα 13: Σύγκριση τάσης κυψέλης καυσίμου για χαμηλό και υψηλό φορτίο μεταξύ της περίπτωσης αναφοράς, του "χειροκίνητου" σχεδιασμού και του βέλτιστου σχεδιασμού.

Συμπεράσματα

Με βάση τα αποτελέσματα που παρουσιάζονται στη διπλωματική αυτή εργασία, προκύπτουν τα ακόλουθα συμπεράσματα :

1. Η τιμή του πορώδους ή της κατανομής αυτού στο GDL πρέπει να αντισταθμίζει την αγωγιμότητα του GDL και την ευκολία της ροής των αντιδρώντων και του υγρού νερού στο GDL. Η βέλτιστη αντιστάθμιση εξαρτάται από την τιμή του φορτίου.
2. Τόσο στην περίπτωση αναφοράς όσο και στον βέλτιστο σχεδιασμό, η ροή εισέρχεται του GDL πολύ κοντά στην είσοδο των καναλιών και εξέρχεται αυτού πολύ κοντά στην έξοδο των καναλιών.
3. Στον βέλτιστο σχεδιασμό η τιμή του πορώδους του GDL μειώνεται αυστηρά από τη BPP στο CL στο υψηλό φορτίο ενώ δεν ισχύει το ίδιο και στο χαμηλό φορτίο.
4. Για χαμηλό φορτίο, η επιβολή κατανομής πορώδους στη διεύθυνση x είναι πιο σημαντική από την επιβολή κατανομής πορώδους στις άλλες δύο διευθύνσεις. Το αντίθετο ισχύει για υψηλό φορτίο όπου οι διευθύνσεις y και z είναι πιο σημαντικές για την κατανομή πορώδους